

NO-A100 873

NONLINEAR EVOLUTION OF THE KELVIN-HELMHOLTZ INSTABILITY
IN THE HIGH LATITUDE IONOSPHERE(U) NAVAL RESEARCH LAB
WASHINGTON DC M J KESKINEN ET AL. 21 DEC 87

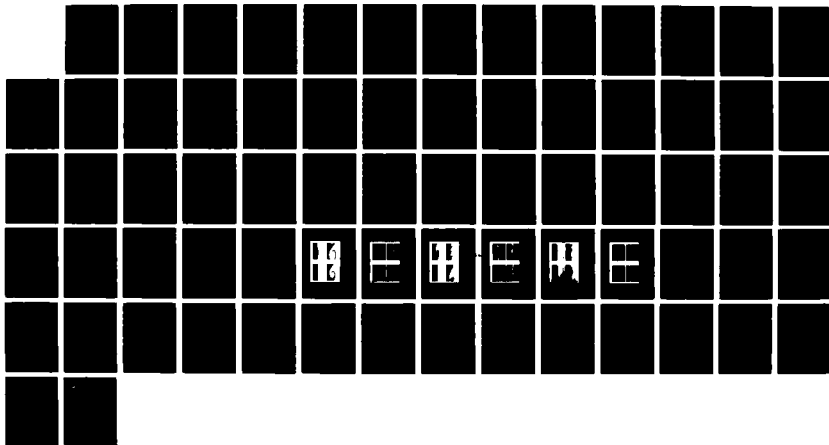
1/1

UNCLASSIFIED

NRL-MR-6043

F/G 4/1

NL



Naval Research Laboratory

Washington, DC 20375-5000

DTIC FILE COPY



2

NRL Memorandum Report 6043

AD-A188 875

Nonlinear Evolution of the Kelvin-Helmholtz Instability in the High Latitude Ionosphere

M.J. KESKINEN, H.G. MITCHELL,* J.A. FEDDER, P. SATYANARAYANA,*
S.T. ZALESK, AND J.D. HUBA

*Geophysical and Plasma Dynamics Branch
Plasma Physics Division*

**Science Applications International Corporation
McLean, VA 22102*

December 21, 1987

This research was partially sponsored by DNA under "Weapons Phenomenology and Code Development," Work Unit Code & Title: RB RC/00158-Plasma Structure Evolution.

DTIC
ELECTE
FEB 02 1988
S E D

Approved for public release, distribution unlimited

88 1 023

SECURITY CLASSIFICATION OF THIS PAGE

REPORT DOCUMENTATION PAGE				Form Approved OMB No 0704 0188	
1a REPORT SECURITY CLASSIFICATION UNCLASSIFIED			1b RESTRICTIVE MARKINGS		
2a SECURITY CLASSIFICATION AUTHORITY			3 DISTRIBUTION AVAILABILITY OF REPORT		
2b DECLASSIFICATION/DOWNGRADING SCHEDULE			Approved for public release; distribution unlimited.		
4 PERFORMING ORGANIZATION REPORT NUMBER(S) NRI. Memorandum Report 6043			5 MONITORING ORGANIZATION REPORT NUMBER(S)		
6a NAME OF PERFORMING ORGANIZATION Naval Research Laboratory		6b OFFICE SYMBOL (If applicable) Code 4780	7a NAME OF MONITORING ORGANIZATION		
6c ADDRESS (City, State, and ZIP Code) Washington, DC 20375-5000			7b ADDRESS (City, State, and ZIP Code)		
8a NAME OF FUNDING/SPONSORING ORGANIZATION ONR, NASA, DNA		8b OFFICE SYMBOL (If applicable)	9 PROGRAM ELEMENT IDENTIFICATION NUMBER		
8c ADDRESS (City, State, and ZIP Code) ONR-800 No. Quincey St. Arlington, VA 22203 NASA-Washington, DC 20546 DNA-Washington, DC 20305			10 SOURCE OF FUNDING NUMBERS		
			PROGRAM ELEMENT NO	PROJECT NO	TASK NO
			(See page ii)	(See page ii)	(See page ii)
11 TITLE (Include Security Classification) Nonlinear Evolution of the Kelvin-Helmholtz Instability in the High Latitude Ionosphere					
12 PERSONAL AUTHOR(S) (See page ii)					
13a TYPE OF REPORT Interim		13b TIME COVERED FROM TO	14 DATE OF REPORT (Year, Month, Day) 1987 December 21		15 PAGE(S) 70
16 SUPPLEMENTARY NOTATION (See page ii)					
17 COSATI CODES			18 SUBJECT TERMS (Continue on reverse if necessary and identify by block number)		
FIELD	GROUP	SUB GROUP	Kelvin-Helmholtz Instability		
			Pedersen conductivity effects		
			Spatial power spectra		
19 ABSTRACT (Continue on reverse if necessary and identify by block number) The nonlinear evolution of the electrostatic Kelvin-Helmholtz instability, resulting from velocity-sheared plasma flows perpendicular to an ambient magnetic field, has been studied including Pedersen conductivity effects (i.e., ion-neutral collisions). We find that the Kelvin-Helmholtz instability develops in a distinctly different manner in the nonlinear regime with Pedersen coupling than without it. Specifically, we show that Pedersen coupling effects, in conjunction with a neutral wind and density gradient, (1) result in an increased time scale for Kelvin-Helmholtz instability wave growth, (2) inhibit Kelvin-Helmholtz vortex formation, (3) lead to nonlinear structures which can be described as "breaking waves," and (4) generate, in the nonlinear regime, small scale turbulence by means of secondary instabilities growing on the primary waves. We have also computed the spatial power spectra of the electrostatic potential and density fluctuations and find that there is a tendency for the potential and density to become shallower when Pedersen conductivity effects are included. We compare our results with recent Dynamics Explorer satellite observations of velocity sheared plasma flows in the high latitude, near-earth space plasma and find good agreement.					
20 DISTRIBUTION AVAILABILITY OF ABSTRACT <input checked="" type="checkbox"/> UNCLASSIFIED/UNLIMITED <input type="checkbox"/> SAME AS RPT <input type="checkbox"/> DTIC USERS			21 ABSTRACT SECURITY CLASSIFICATION UNCLASSIFIED		
22a NAME OF RESPONSIBLE INDIVIDUAL M. J. Koskinen			22b TITLE (Include Accession No.) (202) 767-3134	Code 4780	

DD Form 1473, JUN 86

Previous editions are obsolete.

S/N 0102-LF-014-6603

10. SOURCE OF FUNDING NUMBERS

PROGRAM ELEMENT NO.	PROJECT NO.	TASK NO.	WORK UNIT ACCESSION NO.
ONR 61153N		RR-33-02-44	DN880-024
DNA 62715H		RB RC/00158	DN580-062
NASA W-16-154			

12. PERSONAL AUTHOR(S)

Keskinen, M.J., Mitchell,* H.G., Fedder, J.A., Satyanarayana,* P., Zalesak, S.T. and Huba, J.D.

16. SUPPLEMENTARY NOTATION

*Science Applications International Corporation
McLean, VA 22102

This research was partially sponsored by DNA under "Weapons Phenomenology and Code Development", Work Unit Code & Title: RB RC/00158-Plasma Structure Evolution.

CONTENTS

I.	INTRODUCTION	1
II.	MODEL EQUATIONS AND EQUILIBRIA	4
III.	LINEAR THEORY	12
IV.	NUMERICAL SIMULATIONS	15
V.	POWER SPECTRA	18
VI.	SUMMARY AND CONCLUSIONS	19
	ACKNOWLEDGMENTS	23
	REFERENCES	24
	APPENDIX A	30
	APPENDIX B	33



Accession For	
NTIS CRA&I	<input checked="" type="checkbox"/>
DTIC TAB	<input type="checkbox"/>
Unannounced	<input type="checkbox"/>
Justification	
By	
Distribution	
Availability Codes	
Dist	Availability Codes
A-1	

NONLINEAR EVOLUTION OF THE KELVIN-HELMHOLTZ INSTABILITY IN THE HIGH LATITUDE IONOSPHERE

I. INTRODUCTION

The Kelvin-Helmholtz instability has played an important role in understanding a variety of space and astrophysical phenomena such as the dynamics of comet tails [Ershkovich, 1976; Brandt and Mendis, 1979], the interaction between adjacent streams of different velocities in the solar wind [Parker, 1963; Sturrock and Hartle, 1966; Jokipii and Davis, 1969], low frequency fluctuations in the polar cusps [D'Angelo, 1973; D'Angelo et al., 1974], auroral arc dynamics [Hallinan and Davis, 1970], and the interface between the solar wind and magnetospheric boundary [Dungey, 1955; Parker 1958, Aubry et al., 1971; Lepping and Burlaga, 1979; Southwood, 1968]. Hones et al. [1981] have detected, using ISEE satellite data, vortical structures in the low latitude boundary layer. They show that the helicity and approximate spatial extent are consistent with the Kelvin-Helmholtz instability. Williams [1980] and Sckopke et al. [1981] have observed oscillations of the dayside magnetopause with time scales on the order of several minutes which are consistent with Kelvin-Helmholtz driven waves.

Recently, much experimental [Basu et al., 1987; Weber and Buchau, 1981; Bythrow et al., 1984; Cerisier et al., 1985; Rodriguez and Szuszcwicz, 1984; Curtis et al., 1982; Baker et al., 1986; Vickrey et al., 1980] and theoretical [for recent reviews, see Keskinen and Ossakow, 1983; and Kintner and Seyler, 1985 and references therein] attention has been given to the origin of high latitude ionospheric and magnetospheric

plasma turbulence. The Kelvin-Helmholtz or velocity-shear driven instability can lead to both electric field and density fluctuations in the high latitude near earth space plasma [see, e.g., Kintner and Seyler, 1985]. Studies of velocity-sheared flows in space plasmas can be divided into two groups depending upon whether plasma flow velocities are either parallel [Lerche, 1966; Southwood, 1968; D'Angelo, 1973; Ershkovich, 1979; Gary and Schwartz, 1980; Huba, 1981; Mishin, 1981; Lee et al., 1981; Walker, 1981; Keskinen and Huba, 1983] or perpendicular [Hallinan and Davis, 1970; Miura and Sato, 1978; Miura and Pritchett, 1982; Pritchett and Coroniti, 1984; Thompson, 1983] to the ambient magnetic field. Both cases have been studied in the MHD [Mikhailovskii, 1974; Sen, 1964; Southwood, 1968] and electrostatic [D'Angelo, 1965; Smith and von Goeler, 1968] limits. Furthermore, the velocity, in both cases, is usually taken to vary spatially transverse to the magnetic field in the electrostatic limit. In this study we restrict ourselves to sheared flows perpendicular to the geomagnetic field. Hallinan and Davis [1970] and Webster and Hallinan [1973] have attributed the small scale vortex configurations often seen near auroral arcs [Hallinan and Davis, 1970; Oguti, 1974] to be driven by a transverse Kelvin-Helmholtz or velocity shear driven instability. Kintner [1976] and Kelley and Carlson [1977] have shown that electrostatic wave activity is well correlated with strong transverse velocity shears associated with auroral arcs. Recently, Basu et al. [1987], using Dynamics Explorer satellite data, have measured the spectrum of the electric field and density fluctuations associated with velocity sheared regions near auroral arcs.

Theoretical analyses of the transverse Kelvin-Helmholtz instability in space plasmas have exploited the analogy with crossed-field electron beams in laboratory plasmas [Buneman et al., 1966; Levy and Hockney, 1968] and velocity sheared flows in neutral fluids [Chandrasekhar, 1961; Michalke, 1964; Blumen et al., 1975; Drazin and Davey, 1977]. Miura and

Sato [1978] have studied the transverse Kelvin-Helmholtz instability, using numerical simulations, and its role in auroral arc deformation. Thompson [1983] and Satyanarayana et al. [1987a] have investigated the effects of parallel electron dynamics on the transverse Kelvin-Helmholtz instability. Sydora et al. [1984] have analyzed the possible role of the transverse Kelvin-Helmholtz instability in radially injected plasma clouds. Pritchett and Coroniti [1984] have discussed the collisionless transverse electrostatic Kelvin-Helmholtz instability with inclusion of lowest order finite Larmor radius effects. Recently, Lyons and Walterscheid [1985] discussed the generation of auroral omega bands in terms of a Kelvin-Helmholtz instability in thermospheric neutral wind patterns.

However, the previous theoretical studies have treated the Kelvin-Helmholtz instability as it occurs in a collisionless magnetospheric context with no collisional ionospheric coupling. Due to the relatively long growth times of the Kelvin-Helmholtz instability compared to the Alfvén travel times between the inner magnetosphere and ionosphere, and/or long static electric field mapping distances, ionospheric collisional effects must be considered in a proper description of the Kelvin-Helmholtz instability in the high latitude near-earth space plasma.

In this report, we present the first numerical simulation of the nonlinear evolution of the electrostatic Kelvin-Helmholtz instability with ionospheric Pedersen conductivity coupling. We find that the Kelvin-Helmholtz instability develops in a distinctly different manner in the nonlinear regime with Pedersen coupling than without it. Specifically, we show that Pedersen coupling effects, in conjunction with a neutral wind and density gradient, (1) result in an increased time scale for Kelvin-Helmholtz instability wave growth, (2) inhibit Kelvin-Helmholtz vortex formation, (3) lead to nonlinear structures which can be described as "breaking waves", and (4) generate, in the nonlinear regime, small scale turbulence by means of secondary instabilities growing on primary waves.

We have also computed the spatial power spectra of the electrostatic potential and density fluctuations and find differences with and without Pedersen conductivity effects. For the standard Kelvin-Helmholtz instability with a velocity-shear gradient in the y-direction, but with a density gradient and no ion collisions, we find $P(k_x) \propto k_x^{-5.4 \pm 0.4}$ and $P(k_y) \propto k_y^{-5.3 \pm 0.3}$ for the electrostatic potential fluctuations, and $P(k_x) \propto k_x^{-2.2 \pm 0.3}$ and $P(k_y) \propto k_y^{-2.3 \pm 0.3}$ for the density fluctuations. Here $P(k_x)$ and $P(k_y)$ are the transverse, time and space averaged spatial power spectra. For the Kelvin-Helmholtz instability with a density gradient and including ion collisional effects we find, in general, shallower spectra with $P(k_x) \propto k_x^{-(4.5 - 5.0)}$, and $P(k_y) \propto k_y^{-(5.0 - 5.5)}$ for the potential fluctuations, and with $P(k_x) \propto k_x^{-(1.9 - 2.3)}$ and $P(k_y) \propto k_y^{-(1.5 - 2.0)}$ for the density fluctuations.

The organization of the paper is as follows. In Section 2 we present the basic assumptions of the model, derive the basic model equations, and possible equilibrium configurations. In Section 3 we present a general linear theory of the Kelvin-Helmholtz instability with and without Pedersen coupling effects. In Section 4 we solve the fundamental nonlinear equations, in real configuration space, describing the Kelvin-Helmholtz instability with Pedersen coupling. In Section 5 we discuss the evolution, in k -space, of the Kelvin-Helmholtz instability with and without Pedersen effects. Finally, in Section 6 we summarize our findings and apply our results to velocity sheared configurations in space plasmas.

II. MODEL EQUATIONS AND EQUILIBRIA

We model the evolution of the Kelvin-Helmholtz instability transverse to the ambient geomagnetic field and include lowest order effects of magnetosphere-ionosphere coupling. Since we use the electrostatic approximation, it will be assumed that the time scales of interest in the

problem are long compared to the transit time of an Alfvén wave across the modeled region along the magnetic field. This assumption implies that the plasma is quasi-neutral everywhere and that the electric field perpendicular to the magnetic field maps perfectly along the field within the modeled region. Further, the fact that the electrons have a greater mobility parallel to the magnetic field than the ions allows the assumption that all parallel currents are electron currents and that the ions have no velocity parallel to the field. As a result of these assumptions, the model may be viewed as a set of ion layers perpendicular to the magnetic field representing both ionospheric and magnetospheric contributions, as shown in Fig. 1, which are strongly linked by the mapping of the perpendicular electric field between layers and by the parallel electron currents which flow between layers in order to preserve quasi-neutrality. For simplicity, we will neglect any geometric effects due to field line curvature and assume that the magnetic field $\underline{B} = B \underline{e}_z$ is in the z-direction and constant, so that each ion layer is an xy-plane. This assumption does not prohibit the magnetic field from taking on different magnitudes on different layers, since it is possible to show that the geometry of each layer scales inversely with B, it just allows the local curvature of the perpendicular layer and associated effects (e.g., gradient and curvature drifts) to be neglected.

Quasi-neutrality implies that the electron density is equal to the ion density everywhere, i.e., $n_e = n_i$. Because the electron gyrofrequency is very large compared to the other frequencies in the problem, the electron momentum equation perpendicular to the magnetic field may be reduced to the statement that the electrons are perfectly magnetized and move with the $\underline{E} \times \underline{B}$ velocity within the ion layer:

$$\underline{v}_e = \underline{V} = c\underline{E} \times \hat{e}_z \quad (1)$$

The perpendicular ion flow is not divergence-free, so a parallel electron flux or current is driven along the magnetic field between the ion layers in order to maintain quasi-neutrality. We will neglect dynamic effects arising solely from the parallel dynamics, such as parallel potential drops, so that the parallel electron momentum equation can be neglected since it is redundant with the quasi-neutrality condition. The electron and ion densities are further affected by the recombination rate, but this has no effect on the structure evolution that we are interested in simulating. That is, recombination acts to reduce the plasma population, not to damp the development of structure. As a result, we neglect recombination in our model.

For each layer the governing equations are the continuity and momentum equations for each ion species, i.e.,

$$\frac{\partial n_i}{\partial t} + \underline{\nabla} \cdot n_i \underline{v}_i = 0 \quad (2)$$

$$\frac{1}{Q_i} \left(\frac{\partial}{\partial t} + \underline{v}_i \cdot \underline{\nabla} \right) \underline{v}_i = \left(\frac{c\underline{E}}{B} + \underline{v}_i \times \hat{e}_z \right) + \frac{v_i}{Q_i} (\underline{v}_n - \underline{v}_i) \quad (3)$$

where i denotes the ion species, n_i the ion density, \underline{v}_i the ion velocity, $Q_i = q_i B / cm_i$ the ion cyclotron frequency, m_i the ion mass, q_i the ion charge, ν_i the ion-neutral collision frequency, \underline{v}_n the neutral velocity, c the speed of light, and \underline{E} the electric field. Temperature effects have been neglected in the ion momentum equations and all vector quantities and gradient operators are assumed to be perpendicular to the magnetic field $B\hat{e}_z$. In the following we assume that the ionospheric contribution to our model can be described by an F-layer only in order to isolate and study the

effects of Pedersen conductivity on the Kelvin-Helmholtz instability. Further, we assume that the ion gyrofrequency is large compared to both the ion-neutral collision frequency (F-region approximation) and the characteristic frequency of the Kelvin-Helmholtz instability, so that the ion velocity may be replaced by the $E \times B$ velocity in the small terms in (2), leading to the following expression for the ion velocity when the equation is solved for \underline{v}_i :

$$\underline{v}_i = \underline{V} + \frac{c\nu_i}{B\Omega_i} \left[\underline{E} + \frac{B}{c} \underline{v}_n \times \underline{e}_z \right] + \frac{c}{B\Omega_i} \left[\frac{\partial}{\partial t} + \underline{V} \cdot \underline{\nabla} \right] \underline{E} \quad (4)$$

The ion velocity is therefore equal to the $E \times B$ velocity plus small terms corresponding to the Pedersen drift and the polarization drift. Note that Hall drifts have been neglected in this approximation since they are second order in ν_i/Ω_i . The ion and electron densities are equal by quasi-neutrality, and the ion and electron velocities are both equal to the $E \times B$ velocity to lowest order, so the continuity equation for each level has the form:

$$\frac{\partial n}{\partial t} + \underline{\nabla} \cdot n\underline{V} = 0 \quad \text{where } n \equiv n_e = n_i \quad (5)$$

Equation (5) is an approximation to equation (2), made by neglecting Pedersen and polarization drifts relative to the $E \times B$ drift. This turns out to be a good approximation for the physical situation we are simulating, but it is possible to simulate the full equation (2). The approximation is made here primarily in the interest of simplifying the theoretical discussion.

The perpendicular current density within each layer may be calculated from (3) and (4):

$$\underline{j} = \sigma_p \left[\underline{E} + \frac{B}{c} \underline{v}_n \times \underline{e}_z \right] + \frac{c}{4\pi} \left[\frac{\partial}{\partial t} + \underline{V} \cdot \underline{\nabla} \right] \underline{E} \quad (6)$$

where $\sigma_p = (necv_i/B\Omega_i)$ is the Pedersen conductivity of the layer, $c_M = (c^2/4\pi V_A^2)$ is the inertial capacitance, and $V_A = B/(4\pi m_i)^{1/2}$ is the Alfvén velocity. In order to maintain quasi-neutrality, the divergence of the total current density must be zero, so the perpendicular divergence of this current must be canceled by a parallel divergence in the electron current. If it is assumed that all currents generated within this model must also close within this model, then the field-line integrated divergence of the perpendicular current must be zero, i.e.,

$$\begin{aligned} 0 &= \int dz \underline{\nabla} \cdot \underline{j} = \underline{\nabla} \cdot (\underline{J}_{ped} + \underline{J}_{pol}) \\ &= \underline{\nabla} \cdot \left(\Sigma_p \left[\underline{E} + \frac{B}{c} \underline{v}_n \times \underline{e}_z \right] + C_M \left[\frac{\partial}{\partial t} + \underline{v} \cdot \underline{\nabla} \right] \underline{E} \right) \end{aligned} \quad (7)$$

where \underline{J}_{ped} and \underline{J}_{pol} are the field-line integrated Pedersen and polarization currents, $\Sigma_p = \int \sigma_p dz$ is the field-line integrated Pedersen conductivity, $C_M = \int c_M dz$ is the field-line integrated inertial capacitance, and $\underline{v}_n = (\int \sigma_p \underline{v} dz) / \Sigma_p$ is the conductivity-weighted average neutral velocity along the field line. If we now define ϕ to be the electrostatic potential, i.e., $\underline{E} = -\nabla\phi$, the behavior of the system is defined by an ion continuity equation at each level:

$$\frac{\partial n}{\partial t} + \nabla \cdot \frac{nc}{B} (\hat{e}_z \times \nabla\phi) = 0 \quad (8)$$

and a single potential equation for the electrostatic potential common to all layers:

$$0 = \nabla \cdot \left(\Sigma_p \left[\nabla\phi - \frac{B}{c} \underline{v}_n \times \hat{e}_z \right] + C_M \left[\frac{\partial}{\partial t} + \frac{c}{B} (\hat{e}_z \times \nabla\phi) \cdot \underline{\nabla} \right] \nabla\phi \right). \quad (9)$$

Thus, the plasma on each level $E \times B$ drifts under the influence of the perpendicular electric field, which is itself determined by the fact that the perpendicular Pedersen and polarization drift currents driven by the field must close by means of parallel electron currents within the model.

The Pedersen currents, represented by the first term in (9), tend to reduce any potential which is not supported by the density gradients and the neutral winds, while the polarization drift currents, represented by the second term, tend to slow this decay. As a result, the balance between the effects defines an inertial relaxation rate $\tilde{\nu} = \Sigma_p / C_M$ for changes in the potential.

In order to apply (8) and (9), it is necessary to specify the exact relationship between the density n along the field line and the field-line integrated quantities Σ_p and C_M . In general this is accomplished by separating the configuration into discrete vertical regions with similar characteristics, e.g., a magnetospheric region and an ionospheric region, and treating each region as a single layer. In a previous paper [Mitchell et al., 1985], we defined a magnetospheric layer of constant density and an ionospheric layer with a density gradient unstable to the $E \times B$ instability. In such a case, the magnetospheric continuity equation was not necessary since a uniform density is unchanged by the incompressible $E \times B$ flow field. Therefore, it was necessary to retain only one continuity equation, for the ionospheric density, and the Pedersen conductivity Σ_p in the potential equation was proportional to this density. The capacitance C_M , which is largely due to the cumulative inertia of the particles along the long length of field line in the magnetosphere, became a constant.

In this paper we wish to study the effect that the coupling between magnetospheric polarization drift currents and ionospheric Pedersen currents has on the development of an inertial instability, specifically, the Kelvin-Helmholtz instability which occurs on a velocity shear interface. Once again there is an ionospheric layer contributing the Pedersen conductivity Σ_p and a magnetospheric layer contributing C_M to the

configuration. The velocity shear which excites the instability is present along the entire field line because of the electric field mapping. For the ionospheric layer the shear configuration requires a density gradient in order to be an equilibrium in the presence of Pedersen conductivity. The source of the velocity shear is assumed to be magnetospheric and naturally associated with a density gradient, such as the shear at the plasmopause, so we will assume that there is a density gradient across the shear along the entire field line. This assumption allows us to view the entire field line as a single layer with field-line integrated density $N = \int n \, dz$ and to assume that both the Pedersen conductivity Σ_p and the inertial capacitance C_M are proportional to N . Therefore the relaxation rate $\tilde{\nu}$ is a constant for this model, and the effect of the Pedersen currents on the development of the Kelvin-Helmholtz instability depends on the relationship of the value of this rate to that of the growth rate of the instability. If $\tilde{\nu}$ is much smaller than the growth rate, the model is purely inertial, and if the two rates are comparable, the collisional effects are significant. The explicit form of the continuity and potential equations for this model now take the form

$$\left[\frac{\partial}{\partial t} + \frac{c}{B} (\hat{e}_z \times \nabla \phi) \cdot \nabla \right] N = 0 \quad (10)$$

and

$$0 = \nabla \cdot \left(\tilde{\nu} N \left[\nabla \phi - \frac{B}{c} \frac{V_n}{v_n} \times \hat{e}_z \right] + N \left[\frac{\partial}{\partial t} + \frac{c}{B} (\hat{e}_z \times \nabla \phi) \cdot \nabla \right] \nabla \phi \right), \quad (11)$$

where explicit use of the incompressibility of the $E \times B$ flow has been used in (10).

The basic equilibrium configuration for the Kelvin-Helmholtz instability consists of a velocity shear $V_x(y) \hat{e}_x$ supported by an electric field $\underline{E} = E_y(y) \hat{e}_y$ such that $V_x(y) = cE_y(y)/B$. There are no

polarization currents in this configuration because the gradient of \underline{E} is perpendicular to \underline{V} . If there are no ion-neutral collisions, this configuration will be an equilibrium for any density profile for which $\partial N/\partial x = 0$. In the presence of ion-neutral collisions, the Pedersen conductivity is non-zero and there are Pedersen currents in the y -direction, so that this configuration is an equilibrium only if the divergence of the Pedersen current is zero everywhere, i.e., if $\partial N(y)E_y(y)/\partial y = -\nabla \cdot (N(y)\underline{V}_n \times \underline{B}/c)$. If we make the simplifying assumption that the neutral wind is uniform, the equilibrium condition becomes $\partial [N(y)(E_y(y) - V_{nx}B/c)]/\partial y = 0$. This condition reflects the fact that the Pedersen currents act to short out the electric field associated with the velocity shear on the time scale \bar{v}^{-1} unless the field is supported by the current due the neutral collisions with the ions. Although the equilibrium allows an arbitrary neutral wind component parallel to the density gradient, we will assume that $V_{ny} = 0$, since a parallel neutral component introduces $E \times B$ instability effects into the configuration. An investigation of the $E \times B$ /Kelvin-Helmholtz instability coupling for an arbitrary neutral wind direction will await a later work.

In our calculations we explicitly assume that the equilibrium velocity shear has the form $V_x(y) = -V_0 \tanh(y/L)$ so that the shear in V_x is localized within a scale length L of the origin in y , and V_x is roughly constant outside of this region. This form implies that the equilibrium electric field and density have the forms $E_y(y) = -(BV_0/c) \tanh(y/L)$ and $N(y) = N_0 V_0 / [-V_0 \tanh(y/L) - V_n]$. Note here that the magnitude of V_n must be greater than that of V_0 or there will be a singularity in $N(y)$. The implication is that there must be a non-zero neutral wind in the frame in which the velocity shear is symmetric. The explicit choice of the ratio V_n/V_0 determines the magnitude of the density jump across the velocity

shear, i.e., the value of $N(+\infty)/N(-\infty)$. In the cases we will show here this ratio is taken to be -2 so that $N(+\infty)/N(-\infty) = 3$. Another point is that the anti-symmetric nature of the Kelvin-Helmholtz equilibrium in the y -direction has been broken by the required form of the density gradient. The geometry of the equilibrium we have chosen is shown in Fig. 2. This particular equilibrium is chosen since it simulates, approximately, the plasma configurations along the plasma sheet outer and inner boundaries and its footprints in the polar ionosphere in and near auroral and polar cap arcs.

It is useful to note here that the equilibrium geometry that we have defined occurs naturally in the non-linear development of the $E \times B$ instability. In that instability, a neutral wind blowing down a density gradient causes the gradient to striate in the direction perpendicular to the neutral wind and 'fingers' to grow out of the gradient. The edges of these fingers have the equilibrium geometry defined here, i.e., a velocity shear and associated density gradient perpendicular to a neutral wind. In our previous paper [Mitchell et al., 1985], it was shown that the inclusion of inertial effects in this configuration caused the growth of modes with wave vectors parallel to the neutral wind direction, a result due possibly to Kelvin-Helmholtz-like effects in the finger geometry.

III. LINEAR THEORY

In order to study the linear theory of the growth of the Kelvin-Helmholtz instability within the equilibrium we have defined, the linear perturbation is assumed to have wave number k in the x -direction and frequency ω , so that the quantities N and ϕ may be written:

$$N = N(y) + \delta N(y) e^{i(kx - \omega t)} ; \quad \phi = \phi(y) + \delta \phi(y) e^{i(kx - \omega t)} . \quad (12)$$

By substituting these expressions into (10) and (11), we obtain

$$(\omega - kV_x) \delta N = \frac{kc}{B} \frac{\partial N}{\partial y} \delta \phi \quad (13)$$

and

$$\begin{aligned} & (\omega + i\tilde{\nu} - kV_x) \left(\frac{\partial}{\partial y} (N \frac{\partial}{\partial y} \delta \phi) - Nk^2 \delta \phi \right) \\ & = -k\delta \phi \frac{\partial}{\partial y} \left(N \frac{\partial}{\partial y} V_x \right) - i\frac{\tilde{\nu}B}{c} N (V_n - V_x) \frac{\partial}{\partial y} \left(\frac{\delta N}{N} \right). \end{aligned} \quad (14)$$

Equation (13) can be substituted into (14), yielding the following mode equation for the Kelvin-Helmholtz instability

$$\frac{\partial}{\partial y} \left[A \frac{\partial}{\partial y} \left(\frac{\delta \phi}{\omega - kV_x} \right) \right] = k^2 A \left(\frac{\delta \phi}{\omega - kV_x} \right) \quad (15)$$

where

$$A = \frac{(\omega - kV_x) (\omega + i\tilde{\nu} - kV_x)}{(V_n - V_x)}.$$

For the region outside the shear layer, V_x and A are constant so that (15) reduces to

$$\frac{\partial^2}{\partial y^2} \delta \phi = k^2 \delta \phi, \quad (16)$$

which implies that the perturbation potential has a decay length of $1/k$ in the shear direction.

We have solved (15) analytically (see Appendix A) in the sharp boundary limit and numerically for a smooth boundary profile. For the smooth profile we have taken $V_x = -V_0 \tanh(y/L)$ and the results are plotted in Fig. 3 for the cases $\nu \equiv \tilde{\nu}/(V_0/L) = 0, 0.1, 0.34, 0.5$. The 'classic' Kelvin-Helmholtz case is represented by the upper curve in this figure, and is obtained by setting $\tilde{\nu} = 0$ and assuming $V_n \gg V_x$ in (15). The latter

assumption reduces the background density gradient to zero. In this case the growth rate γ (where $\omega = \omega_r + i\gamma$) has a maximum value of $\gamma = 0.19 V_0/L$ at $kL = 0.44$. For k less than this value, the growth rate is reduced because the width of the shear region L is small compared to the decay length $1/k$ of the potential in the shear direction, and, for k greater than this value, the growth rate is reduced because the effective shear within the length $1/k$ is small. This case is symmetric in the shear direction so the phase velocity ω_r/k of the instability is zero. The addition of a 3:1 density gradient across the velocity shear ($V_n/V_0 = 2$) reduces the maximum growth rate by about 10%, and produces an asymmetry in the shear direction, resulting in a real phase velocity $\omega_r/k = -.13 V_0$. A 10:1 density gradient ($V_n/V_0 = 1.22$) reduces the maximum growth rate by 50% [Satyanarayana et al., 1987b].

The inclusion of Pedersen conductivity further reduces the growth rate of the instability. From (15) it can be seen that the growth rate of the instability depends solely on the behavior of the function A . This function may also be written

$$A = \left[(\omega + \frac{i}{2} \tilde{\nu} - kV_x)^2 - \frac{1}{4} \tilde{\nu}^2 \right] (V_n - V_x)^{-1} \quad (17)$$

If $\tilde{\nu}$ is small compared to kV_x , $\tilde{\nu}$ is negligible in this equation, and the growth rate is reduced by a factor of $\tilde{\nu}/2$ from the collisionless case. This can be seen in the plots of growth rate for the collisional cases $\nu = \tilde{\nu}/(V_0/L) = 0.10, 0.34, \text{ and } 0.50$ in Fig. 3. The growth rate is reduced by a significant amount when $\tilde{\nu}$ becomes comparable to the collisionless growth rate (about $.2 V_0/L$), and the instability is effectively damped for $\tilde{\nu} > 0.5 V_0/L$. As the density gradient is increased, the growth rate for all of the cases is decreased. We find good agreement between the growth rate as derived from the sharp boundary analysis in the small wavenumber limit, as outlined in Appendix A, and that computed numerically from Eq. (15).

IV. NUMERICAL SIMULATIONS

In our numerical simulation of the evolution of the Kelvin-Helmholtz configuration that we have described, the calculation is performed on a 64×100 cell grid (x,y) which is periodic in the x -direction and has Dirichlet boundary conditions in the y -direction (potential set equal to a constant at the boundaries). In the x -direction, the cell size is uniform and contains one wavelength of the unstable perturbation for the Kelvin-Helmholtz instability within the 64 cells. The y -direction cell size is uniform for the 80 cells covering the interior region from $y = -2L$ to $+2L$, with the 10 boundary cells on either end being a stretched mesh to $y = -13L$ and $+13L$. The aspect of the cells in the uniform mesh region is 4:1 for the wavelength used. The numerical method used to simulate (10) and (11) is described in Zalesak et al. [1982]. The continuity equation is solved numerically using the multidimensional flux-corrected transport techniques of Zalesak [1979], while the potential equation is solved with the incomplete Cholesky conjugate gradient algorithm of Hain [1980].

We have performed three Kelvin-Helmholtz simulations with this model, all of which have a 3:1 density jump and a wavenumber of $k_0 = 0.44/L$. The three cases have scaled inertial relaxation rates of $\nu = 0.00, 0.10,$ and 0.34 , and are represented by the dots on the linear growth rate curves of Fig. 3. These three cases have linear growth rates of $\gamma/(V_0/L) = 0.17, 0.12,$ and 0.03 , respectively, which are close to the maximum growth rates for their respective values of ν . The simulations are initialized with the appropriate eigenfunction for this mode, determined by a numerical eigenfunction code, so that the linear behavior of the two-dimensional electrostatic code may be verified. The eigenfunctions for these three cases are plotted in Fig. 4. The amplitude and phase of the Fourier components $\delta\phi$ are shown in Fig. 4a and 4b, respectively, and the full 2-dimensional eigenfunctions are contoured in Fig. 4c. For each case the eigenfunction has a phase shift within the shear region about the origin.

with the total phase shift increasing from about 1 radian for $\nu = 0.00$, to about 1.6 radians for $\nu = 0.34$.

The behavior of the densities and potentials for the three simulations are displayed in Figs. 5 - 7. In the plot of the $\nu = 0.00$ simulation, the density gradient serves primarily as a tracer for a standard Kelvin-Helmholtz simulation. The initial shear boundary perturbation grows in amplitude and width until the width is on the order of the shear scale size, at which time the boundary layer forms the characteristic vortices and spirals of the Kelvin-Helmholtz instability (shown in the last panel of Fig. 5a). In our simulation, numerical effects begin to diffuse small scale structure when the width of the boundary spiral approaches the cell size. This occurs at roughly time $8t$ in our simulation.

The $\nu = 0.10$ simulation is shown in Figs. 6a and 6b. The linear phase of this simulation is similar to the $\nu = 0.00$ case. When the vortices begin to form, however, the Pedersen conductivity acts to prevent curling of the density contours, and the contours trail out from the perturbation as the perturbation convects to the left. Since the structure is now elongated in the x-direction, it becomes unstable to the Kelvin-Helmholtz instability on this new interface. Smaller scale instabilities due to this effect are evident in the last panel of Fig. 6a. In addition, the leftward convecting perturbation structure overtakes the trailing density structure,

$$P(k_x) = \sum_{k_y} \langle |f_{k_x, k_y}|^2 \rangle$$

$$P(k_y) = \sum_{k_x} \langle |f_{k_x, k_y}|^2 \rangle$$

We now give selected power spectra for the cases $\nu = 0.00$, 0.10 , and 0.34 .

The typical temporal evolution of the potential Fourier modes for several values of k_x is shown in Fig. 8 for the $\nu = 0.00$ case. The

amplitude of the dominant growing mode $k_x = k_0$ increases exponentially until nonlinear effects become important and the mode reaches a saturation level. Agreement between the theoretical value of the linear growth rate and measured value is excellent. In all three cases, $\nu = 0.00, 0.10, 0.34$, our simulations match the predicted linear growth rate for 2 to 4 growth times after initialization. The higher harmonics ($2k_0, 3k_0$, etc.) increase in amplitude at a faster rate until saturation since they are driven by the dominant mode. At saturation the modes oscillate in amplitude as they exchange energy with each other.

Figures 9 and 10 give the time and transverse averaged power spectra of the potential $\delta\phi = \phi - \phi_0$ and density $\delta N = N - N_0$, respectively, for the case $\nu = 0.00$. The wavenumbers k_x and k_y are in units of $k_{0x} = 2\pi/L_x = 0.5/L$ and $k_{0y} = 2\pi/L_y = 1.6/L$, respectively, where L_x is the length of the system in the x direction, L_y is the length of system in the uniform mesh region in the y-direction, and L is the half-width of the shear layer. We find $P(k_x) \propto k_x^{-5.4 \pm 0.4}$ and $P(k_y) \propto k_y^{-5.3 \pm 0.3}$ for $|\delta\phi|^2$ and $P(k_x) \propto k_x^{-2.2 \pm 0.2}$ and $P(k_y) \propto k_y^{-2.3 \pm 0.3}$ for $|\delta N|^2$. The spectra $P(k_x)$ for the potential $\delta\phi$ is in approximate agreement with that computed in the work of Miura and Sato (1978) which showed $|\delta\phi(k_x, y = \text{const.})|^2 \propto k_x^{-6}$. Our measured and multiple overlapping structures are created with smaller y-direction scales than in the previous case. The resulting non-linear structure of the instability is significantly different from the $\nu = 0.00$ simulation, even though the linear growth rates differ only by about 30 percent.

The nonlinear behavior of the $\nu = 0.34$ case is again different from the two preceding cases. In this simulation, density contours are inhibited from curling very early in the development of the instability, and so the y-direction extent of the perturbation is reduced. Density is swept off the high density peak and opposite to the direction of the phase velocity, resulting very quickly in a smaller scale structure parallel to the shear direction than in either of the other simulations. The density plots in

Fig. 7a clearly show the increased small-scale structure and reduced y-extent in the nonlinear development of the instability. In Fig. 7b, the potential plots exhibit only small deviations from equilibrium relative to the behavior in the other two simulations.

V. POWER SPECTRA

We have computed the spatial power spectra of the density and potential fluctuations associated with the evolution of the Kelvin-Helmholtz instability both with and without Pedersen coupling.

We consider a two-dimensional spatial Fourier representation

$$f(x, y, t) = \sum_{k_x, k_y} f_{k_x, k_y}(t) \exp[i(k_x x + k_y y)]$$

with $f = N, \phi$. Here, f_{k_x, k_y} are the Fourier coefficients defined by

$$f_{k_x, k_y} = (2\pi^2)^{-1} \int dx dy f(x, y) \exp[-i(k_x x + k_y y)]$$

The transverse averaged power spectra $P(k_x)$ and $P(k_y)$ are defined by $P(k_x)$ for $\delta\phi$ is shallower since we are essentially integrating $|\delta\phi|^2$ over k_y . In addition, Miura and Sato's spectral results are not time averaged and are obtained using different initial conditions.

In Figs. 11 and 12 we give the power spectra of the perturbation potential $\delta\phi$ and density δN , respectively, for the case $\nu = 0.10$. We have time-averaged the spectra computed in the nonlinear regime over a time interval of approximately five linear growth times after saturation has occurred. The two-dimensional power spectra $|f_{k_x, k_y}|^2$, with $f = N, \phi$, are computed at twenty different, successive times in this interval and then averaged. This averaging minimizes numerically induced fluctuations and gives a more accurate representation of the turbulence spectrum in the saturated, nonlinear regime. We obtain, for $|\delta\phi|^2$, $P(k_x) \propto k_x^{-4.7 \pm 0.2}$

and $P(k_y) \propto k_y^{-5.3 \pm 0.2}$ while for $|\delta N|^2$, $P(k_x) \propto k_x^{-1.9 \pm 0.2}$ and $P(k_y) \propto k_y^{-1.6 \pm 0.2}$. We note that these spectra are shallower compared to the previous case with $\nu = 0.00$.

Figures 13 and 14 display the power spectra of $\delta\phi$ and δN , respectively, for $\nu = 0.34$. For $\delta\phi$, we find $P(k_x) \propto k_x^{-4.6 \pm 0.2}$ and $P(k_y) \propto k_y^{-5.3 \pm 0.2}$. For δN , we obtain $P(k_x) \propto k_x^{-2.1 \pm 0.2}$ and $P(k_y) \propto k_y^{-1.7 \pm 0.3}$. These spectral slopes are also shallower than the $\nu = 0$ case as shown in Figs. 9 and 11.

The spectral indices of the power spectra of the total electrostatic potential ϕ and density N are listed in Table I and display similar values.

In general, we find shallower power spectra for the $\nu = 0.10, 0.34$ cases as opposed to the $\nu = 0.00$ case. We feel that this effect is caused, in part, by the excitation of shorter wavelength (higher k) potential fluctuations by secondary Kelvin-Helmholtz instabilities, as noted in Sec. IV, in the nonlinear regime thus, increasing the power at higher k , and, as a result, shallowing the spectra. We give a simple argument for this shallowing of the spectra based on the lowest order nonlinear evolution of the Kelvin-Helmholtz instability in Appendix B. Also, in addition to the enhanced power at short wavelengths, we note that there is a strong reduction of power at long wavelengths, i.e., small k , for the collisional cases. For example, there is an order of magnitude reduction in the power at $k_y^2 = 4$ for $\nu = 0.34$ (Fig. 16b) from $\nu = 0.00$ (Fig. 12b). This is because the large-scale vortices (or structures) which form in the inertial regime ($\nu = 0.00$) and cause the enhanced power at long wavelengths are suppressed in the collisional regime ($\nu = 0.34$) which therefore leads to a decrease in the power at long wavelengths.

VI. SUMMARY AND CONCLUSIONS

In this paper we have studied, using both analytical and numerical simulation techniques, the linear and nonlinear evolution of the

electrostatic Kelvin-Helmholtz instability, resulting from velocity-sheared plasma flows perpendicular to a magnetic field, including Pedersen conductivity effects. We find that the Kelvin-Helmholtz instability develops, in the nonlinear regime, in a distinctly different manner when Pedersen conductivity effects are included than the case where there is no Pedersen conductivity (i.e., no ion collisions). We find that Pedersen coupling effects, in conjunction with a neutral wind and plasma density gradient, (1) lead to smaller growth rates (increased time scales), in the linear phase of the Kelvin-Helmholtz instability, (2) inhibit Kelvin-Helmholtz vortex formation, (3) lead to nonlinear structures which can be described as "breaking waves", and (4) generate, in the nonlinear regime, small scale structure and turbulence by means of secondary Kelvin-Helmholtz instabilities growing on primary Kelvin-Helmholtz driven waves. We have also computed the spatial power spectra of the electrostatic potential and density fluctuations associated with the Kelvin-Helmholtz instability and find differing spectra with and without Pedersen conductivity effects. For the standard Kelvin-Helmholtz velocity sheared configuration $\underline{V} = V_x(y) \hat{e}_x$, but with a density gradient $n_0(y)$ perpendicular to the velocity flow, we find $P(k_x) \propto k_x^{-5.4 \pm 0.4}$ and $P(k_y) \propto k_y^{-5.3 \pm 0.3}$ for the electrostatic potential fluctuations, and $P(k_x) \propto k_x^{-2.2 \pm 0.3}$ and $P(k_y) \propto k_y^{-2.3 \pm 0.3}$ for the density fluctuations, where $P(k_x)$ and $P(k_y)$ are the time-averaged, spatial power spectra averaged over the y- and x-directions, respectively. For the Kelvin-Helmholtz instability with a density gradient but including ion-neutral collisional effects (Pedersen coupling) we find, in general, shallower spectra with $P(k_x) \propto k_x^{-(4.5-5)}$ and $P(k_y) \propto k_y^{-(5-5.5)}$ for the potential fluctuations with $P(k_x) \propto k_x^{-(1.9-2.3)}$ and $P(k_y) \propto k_y^{-(1.5-2)}$ for the density fluctuations.

Recently, Basu et al. [1987], using Dynamics Explorer satellite data, have measured the simultaneous density and electric field fluctuation spectra associated with velocity shears in both the southern and northern

auroral oval. In this region they observe strong shear when $\Sigma_H \geq \Sigma_p$ and moderate shear when $\Sigma_H \lesssim \Sigma_p$ where $\Sigma_H(\Sigma_p)$ is the approximate integrated Hall (Pedersen) conductivity. In the moderate velocity shear region they find shears $V/L = 1 \text{ sec}^{-1}$ (where $V \sim 1 \text{ km/sec}$ and $L \sim 1 \text{ km}$), and Pedersen conductivities $\Sigma_p = 1 - 5 \text{ mhos}$. Taking a typical $C_m = 10 \text{ farad}$ where C_m is defined in Section 2 we find $v = (\Sigma_p/C_m)/(V_0/L) = 0.1 - 0.5$ which includes the values selected for v in Section 3 and 4. In the velocity shear region Basu et al. [1987] compute the transverse averaged power spectra $|E(k_s)|^2 \propto k_s^{-p}$, $p = 2.8 - 3.6$ and $|n(k_s)|^2 \propto k_s^{-p}$, $p = 1.7 - 2$ where $E(n)$ denotes the electric field (density). Here s denotes the direction of the satellite as it passes through the velocity sheared region. Taking $E(k) \propto k\phi(k)$ this gives for the potential fluctuations $|\phi(k_s)|^2 \propto k_s^{-p}$, $p = 4.8 - 5.6$. It is difficult to relate k_s to the coordinate system used in the simulations of Sec. 4 since the initial conditions for the assumed Kelvin-Helmholtz fluctuations in the ionosphere, as observed by satellites, are not known. The observations of Basu et al. [1986] show velocity shear gradients along the satellite track suggesting that $k_s = k_y$ (direction of velocity gradient at $t = 0$ in the simulations of Sec. 4). Taking $k_s = k_y$ the observed spectral indices for the electric field (potential) and density are in reasonable agreement with those computed from the simulations of Section 4 where we found, for $v = 0.10, 0.34$, $P(k_y) \propto k_y^{-(5.0 - 5.4)}$ for the potential and $P(k_y) \propto k_y^{-(1.6 - 2.0)}$ for the density. Our results are for k_x and k_y in the range $0.5 - 5 \text{ km}^{-1}$ and $1.6 - 16 \text{ km}^{-1}$, respectively, or for scale sizes in the range $12.4 \text{ km} - 1.2 \text{ km}$ and $3.9 - 0.39 \text{ km}$, respectively. Exact agreement can not be expected since we have not included Hall conductivity, parallel potential drops, and three-dimensional effects in our simulations.

On larger spatial scales our simulation results approximate plasma conditions along the magnetospheric tail plasma sheet outer and inner boundaries, and its footprints in the polar ionosphere, the auroral oval.

Figure 15 is a sketch of these regions. At the poleward boundary of the plasma sheet - auroral oval velocity shear is developed between the tailward convection of plasma across the polar cap and the sunward convection at lower latitudes in the auroral oval and the inner plasma sheet. There is also a strong density gradient across the shear boundary from the very low densities of the ionospheric polar cap and magnetic tail lobe to the increased density in the ionospheric auroral plasma and the plasma sheet. The section of the boundary A - A' shown in Fig. 15 (panels a and b) is similar to the shear layer model in this simulation.

The section of the boundary B - B' shown in Fig. 15 (panels a and c) also exhibits a velocity shear layer. Here the shear is developed between the sunward convection in the auroral oval and plasma sheet and the slowly convecting plasma at lower latitudes in the ionosphere and closer to the earth in the magnetotail. Again in these regions a density gradient exists across the shear layer from low latitude plasma toward higher latitude plasma. In order to assess the efficiency of the Kelvin-Helmholtz instability for the plasma sheet - auroral region boundary, it is necessary to estimate the quantities C_m and Σ_p in these regions. For a moderately disturbed nightside auroral oval the conductivity, Σ_p , is typically 5 - 10 mhos. For the outer plasma sheet we estimate C_m to be about 600 farads, taking the density to be 1 cm^{-3} , the average field strength to be 5 nT, and a typical integration length of 10^4 km. For the inner plasma sheet C_m is considerably smaller and about 10 farads, taking the density as 1 cm^{-3} , the field strength as 30 nT, and again a typical integration length of 10^4 km. For shear frequencies $V_0/L \sim 0.1 - 1.0 \text{ sec}^{-1}$ the quantities estimated above would indicate that the high latitude auroral zone - plasma sheet shear boundary should be unstable to the Kelvin-Helmholtz shear instability with only moderate modifications by the ionospheric conductivity because $v \leq 0.1$. On the other hand the low latitude auroral - inner plasma sheet shear boundary should be strongly affected by the ionospheric conductivity

because $\nu \geq 0.5$, and it may be only marginally unstable depending on the precise balance between plasma inertia and conductivity. Figure 16, a sketch of the auroral morphology from Akasofu [1976], shows this general behavior with a very highly irregular and structured poleward boundary and a much less disturbed boundary at lower latitude.

Finally, we wish to point out that our simulation model for simplicity has not included Hall conductivity, parallel potential drops and associated imperfect magnetospheric-ionospheric coupling, variations along the geomagnetic field, and recombination terms. As a consequence, our results are not strictly applicable to the auroral zone plasma. It was our intention to isolate and study only the effects of Pedersen conductivity on the Kelvin-Helmholtz instability as it may occur in the high latitude ionosphere and inner magnetosphere. It is clear that effects such as Hall conductivity and parallel electric fields are important in the auroral regions, and we intend to study their effects on the evolution of Kelvin-Helmholtz instability in space plasmas with more realistic and self-consistent magnetosphere-ionosphere coupling in future studies.

ACKNOWLEDGMENTS

We wish to thank R.A. Heelis and N. Maynard of the Dynamics Explorer science team and Su. Basu for useful discussions concerning experimental data. In addition, we express our thanks to S.I. Akasofu for providing Fig. 16. We also acknowledge useful referee comments and criticisms. This work was supported by NASA, DNA, and ONR.

REFERENCES

- Akasofu, S.-I., Recent progress in studies of DMSP auroral photographs, Space Sci. Rev. 19, 169, 1976.
- Aubry, M.P., M.G. Kivelson, and C.T. Russell, Motion and structure of the magnetopause, J. Geophys. Res., 76, 1673, 1971.
- Baker, K.D., R.A. Greenwald, A.D.M. Walker, P.F. Bythrow, L.J. Zanetti, T.A. Potemra, D.A. Hardy, F.J. Rich, and C.L. Rino, A case study of plasma processes in the dayside cleft, J. Geophys. Res. (1986), in press.
- Basu, Su, S. Basu, C. Senior, D. Weimer, E. Nielsen, and P.F. Fougere, Velocity shears and sub-km scale irregularities in the nighttime auroral F-region, Geophys. Res. Lett., 13, 101, 1986.
- Basu, Su, S. Basu, E. MacKenzie, P.F. Fougere, W.R. Coley, N. Maynard, J.D. Winningham, M. Sugiura, W.B. Hanson, and W.R. Hoegy, Simultaneous density and electric field fluctuation spectra associated with velocity shears in the auroral oval, J. Geophys. Res. (submitted), 1987.
- Blumen, W., P.G. Drazin, and D.F. Billings, Shear layer instability of an inviscid compressible fluid, 2, J. Fluid Mech., 71, 305, 1975.
- Brandt, J.C. and D.A. Mendis, The interaction of the solar wind with comets, in Solar System Plasma Physics, vol. 2, edited by C.F. Kennel et al., p. 253, North-Holland, Amsterdam, 1979.
- Buneman, O., R. Levy II, and L. Linson, The stability of crossed field electron beams, J. Appl. Phys., 37, 3202, 1966.
- Bythrow, P.F., T.A. Potemra, W.B. Hanson, L.J. Zanetti, C.-I. Meng, R.E. Huffman, F.J. Rich, and D.A. Hardy, Earthward directed high-density Birkeland currents observed by HILAT, J. Geophys. Res., 89, 9114, 1984.

- Cerisier, J.C., J.J. Berthelier, and C. Beghin, Unstable density gradients in the high latitude ionosphere, Radio Sci., 20, 755, 1985.
- Chandrasekhar, S., Hydrodynamic and Hydromagnetic Stability, Clarendon, Oxford, 1961.
- Curtis, S.A., W.R. Hoegy, L.H. Brace, N.C. Maynard, M. Sugiura, and J.D. Winningham, DE-2 cusp observations: role of plasma instabilities in topside ionospheric heating and density fluctuations, Geophys. Res. Lett., 9, 997, 1982.
- D'Angelo, N., Kelvin-Helmholtz instability in a fully ionized plasma in a magnetic field, Phys. Fluids, 8, 1748, 1965.
- D'Angelo, N., Ultralow frequency fluctuations at the polar cusp boundaries, J. Geophys. Res., 79, 3129, 1973.
- D'Angelo, N., N.A. Bahnsen, and H. Rosenbauer, Wave and particle measurements at the polar cusp, J. Geophys. Res., 79, 3129, 1974.
- Drazin, P.G. and A. Davey, Shear layer instability of an inviscid compressible fluid, 3, J. Fluid Mech., 82, 255, 1977.
- Dungey, J.W., Electrodynamics of the outer atmosphere, in Proceedings of the Ionosphere, p. 225. The Physical Society of London, London, 1955.
- Ershkovich, A.I., Solar wind interaction with the tail of comet Kohoutek, Planet. Space Sci., 24, 287, 1976.
- Gary, S.P. and S.J. Schwartz, An electrostatic flow shear instability, J. Geophys. Res., 85, 2978, 1980.
- Hain, K., A non-recursive incomplete Cholesky decomposition method for the solution of linear equations with a sparse matrix, NRL Memorandum Report 4264, Naval Research Laboratory, Washington, DC, 1980.
- Hallinan, T.J. and T.N. Davis, Small scale auroral arc distortions, Planet. Space Sci., 18, 1735-1744, 1970.

- Hones, E.W., Jr., J. Birn, S.J. Bame, J.R. Asbridge, G. Paschmann, N. Scopke, and G. Haerendel, Further determination of the characteristics of magnetospheric plasma vortices with ISEE 1 and 2, J. Geophys. Res., 86, 814, 1981.
- Huba, J.D., Stabilization of the electrostatic Kelvin-Helmholtz instability in high β plasmas, J. Geophys. Res., 86, 8991, 1981.
- Jokipii, J.R. and L. Davis, Jr., Long-wavelength turbulence and the heating of the solar wind, Astrophys. J., 156, 1101, 1969.
- Kelley, M.C. and C.W. Carlson, Observations of intense velocity shear and associated electrostatic waves near an auroral arc, J. Geophys. Res., 82, 2343-2348, 1977.
- Keskinen, M.J. and S.L. Ossakow, Theories of high-latitude ionospheric irregularities: a review, Radio Science, 18, 1077, 1983.
- Keskinen, M.J. and J.D. Huba, Generation of lower hybrid waves by inhomogeneous electron beams, J. Geophys. Res., 88, 3109, 1983.
- Kintner, P.M., Jr., Observations of velocity shear driven plasma turbulence, J. Geophys. Res., 81, 5114-5122, 1976.
- Kintner, P.M. and C.E. Seyler, The status of observations and theory of high latitude ionospheric and magnetospheric plasma turbulence, Space Sci. Rev., 40, 1123, 1985.
- Lee, L.C., R.K. Albano, and J.R. Kan, Kelvin-Helmholtz instability in the magnetopause-boundary layer region, J. Geophys. Res., 86, 54, 1981.
- Lepping, R.P. and L.F. Burlaga, Geomagnetopause surface fluctuations observed by Voyager 1, J. Geophys. Res., 84, 7099, 1979.
- Lerche, I., Validity of the hydromagnetic approach in discussing instability of the magnetospheric boundary. J. Geophys. Res., 71, 2365, 1966.

- Levy, R.H. and R.W. Hockney, Computer experiments on low density cross-field electron beams, Phys. Fluids, 11, 766-771, 1968.
- Lyons, L.R. and R.L. Walterscheid, Generation of omega bands by shear instability of the neutral winds, J. Geophys. Res., 90, 12321, 1985.
- Michalke, A., On the inviscid instability of the hyperbolic-tangent velocity profile, J. Fluid Mech., 19, 543-556, 1964.
- Mikhailovskii, A.B., Theory of Plasma Instabilities, Plenum, New York, 1974.
- Mishin, V.V., On the MHD instability of the earth's magnetopause and its geophysical effects, Planet. Space Sci., 29, 359, 1981.
- Mitchell, H.G., J.A. Fedder, M.J. Keskinen, and S.T. Zalesak, A simulation of high latitude F-layer instabilities in the presence of magnetosphere-ionosphere coupling, Geophys. Res. Lett., 12, 283, 1985.
- Miura, A. and T. Sato, Shear instability: auroral arc deformation and anomalous momentum transport, J. Geophys. Res., 83, 2109, 1978.
- Miura, A. and P.L. Pritchett, Nonlocal stability analysis of the MHD Kelvin-Helmholtz instability in a compressible plasma, J. Geophys. Res., 87, 7431, 1982.
- Oguti, T., Rotational deformations and related drift motions of auroral arcs, J. Geophys. Res., 79, 3861-3865, 1974.
- Parker, E.N., Dynamics of the interplanetary gas and magnetic fields, Astrophys. J., 128, 6640, 1958.
- Parker, E.N., Interplanetary Dynamical Processes, Interscience, New York, 1963.
- Pritchett, P.L. and F.V. Coroniti, The collisionless macroscopic Kelvin-Helmholtz instability 1. Transverse electrostatic mode, J. Geophys. Res., 89, 168, 1984.

- Rodriguez, P. and E. Szuszczewicz. High latitude irregularities in the lower F-region: intensity and scale size distribution, J. Geophys. Res., 89, 5575, 1984.
- Satyanarayana, P., Y.C. Lee, and J.D. Huba, Transverse Kelvin-Helmholtz instability with parallel electron dynamics and Coulomb collisions, J. Geophys. Res., (in press), 1987a.
- Satyanarayana, P., Y.C. Lee, and J.D. Huba, On the stability of a stratified shear layer, Phys. Fluids, 30, 81, 1987.
- Skopke, N., G. Paschmann, G. Haerendel, B.U.O. Sonnerup, S.J. Bame, T.G. Forbes, E.W. Hones, Jr., and C.T. Russell, Structure of the low-latitude boundary layer, J. Geophys. Res., 86, 2099, 1981.
- Sen, A.K., Stability of hydromagnetic Kelvin-Helmholtz discontinuity, Phys. Fluids, 7, 1293, 1964.
- Smith, C.G. and S. von Goeler, Kelvin-Helmholtz instability for a collisionless plasma model, Phys. Fluids, 11, 2665, 1968.
- Southwood, D.J., The hydromagnetic stability of the magnetospheric boundary, Planet. Space Sci., 16, 587, 1968.
- Sturrock, P.A. and R.E. Hartle, Two-fluid model of the solar wind, Phys. Rev. Lett., 16, 628, 1966.
- Sydora, R.D., J.S. Wagner, L.C. Lee, E.M. Wescott, and T. Tajima, Electrostatic Kelvin-Helmholtz instability in a radially injected plasma cloud, Phys. Fluids, 27, 1565, 1984.
- Thompson, W.B., Parallel electric fields and shear instabilities, J. Geophys. Res., 88, 4805, 1983.
- Vickrey, J.F., C.L. Rino, and T.K. Potemra, Chathamia Triad observations of unstable ionization enhancement in the lower F-region, Geophys. Res. Lett., 7, 39, 1980.

- Walker, A.D.M., The Kelvin-Helmholtz instability in the low latitude boundary layer, Planet. Space Sci., 29, 1119, 1981.
- Weber, E.J. and J. Buchau, Polar cap F layer auroras, Geophys. Res. Lett., 8, 125, 1981.
- Webster, H.F. and T.J. Hallinan, Instabilities in charge sheets and current sheets and their possible occurrence in the aurora, Radio Sci., 8, 475-482, 1973.
- Williams, D.J., Magnetopause characteristics at 0840-1040 hours local time, J. Geophys. Res., 85, 3387, 1980.
- Zalesak, S.T., Fully multidimensional flux-corrected transport algorithms for fluids, J. Comp. Phys., 31, 335, 1979.

APPENDIX A

We present a linear analysis of (15)

$$\frac{\partial}{\partial y} \left[A \frac{\partial}{\partial y} \left(\frac{\delta\phi}{\omega - kV_x} \right) \right] = k^2 A \left(\frac{\delta\phi}{\omega - kV_x} \right) \quad (\text{A1})$$

where $A = (\omega - kV_x)(\omega + i\tilde{\nu} - kV_x)/(V_n - V_x)$ for the case of a velocity profile with a sharp boundary, i.e., $kL_v \ll 1$. The velocity profile is taken to be

$$V_x = \begin{cases} V_+ & y > 0 \\ V_- & y < 0 \end{cases} \quad (\text{A2})$$

This analysis is best suited for long wavelength modes, $kL_v \ll 1$. We also compare the analytical results with the exact numerical solutions of (A1); the numerical solutions pertain to flows with smooth profiles (hyperbolic tangent) with finite thickness of the shear layer.

First, we rewrite (A1), by defining $\Phi \equiv \delta\phi/(\omega - kV_x)$, as

$$\frac{\partial}{\partial y} \left[A \frac{\partial \Phi}{\partial y} \right] = k^2 A \Phi \quad (\text{A3})$$

For $|y| \rightarrow \infty$, we have

$$\frac{\partial^2 \Phi}{\partial y^2} = k^2 \Phi \quad (\text{4})$$

so that

$$\Phi = C_1 e^{ky} + C_2 e^{-ky} \quad (\text{A5})$$

and

$$\Phi = a_+ e^{-ky} \text{ for } y > 0. \quad (\text{A6})$$

We integrate (A3) across the layer to obtain the matching conditions at $y = 0$. On integrating once we obtain

$$\left[A \frac{\partial \Phi}{\partial y} \right]_{-\varepsilon}^{\varepsilon} = \int_{-\varepsilon}^{\varepsilon} dy k^2 A \Phi \quad (\text{A7})$$

and after integrating once again

$$\Phi \Big|_{-\varepsilon}^{\varepsilon} = \int_{-\varepsilon}^{\varepsilon} dy A^{-1} \int_{-\varepsilon}^{\varepsilon} dy k^2 A \Phi \quad (\text{A8})$$

We substitute (A5) and (A6) into (A7) and (A8) and let $\varepsilon \rightarrow 0$. The right hand sides of (A7) and (A8) vanish for $\varepsilon \rightarrow 0$ with the result

$$A_+ a_+ + A_- a_- = 0 \quad (\text{A9})$$

$$a_+ - a_- = 0 \quad (\text{A10})$$

Using the definition of A , (A9) and (A10) we obtain the dispersion equation

$$\frac{(\omega + i\tilde{\nu} - kV_+)(\omega - kV_+)}{(V_n - V_+)} = - \frac{(\omega + i\tilde{\nu} - kV_-)(\omega - kV_-)}{(V_n - V_-)} \quad (\text{A11})$$

For the special case of $V_+ = -V_- = V_0$, (A11) becomes

$$\omega = -i\tilde{\nu}/2 + kV_0^2/V_n \pm \left[-\tilde{\nu}^2/4 - k^2V_0^2(1 - V_0^2/V_n^2) \right]^{1/2} \quad (\text{A12})$$

from which

$$\omega_1 = 1 - \frac{\tilde{\nu}}{2} - \frac{V_0^2}{V_n} \quad (\text{A13})$$

$$\gamma = \frac{\tilde{\nu}}{2} \pm \left[\tilde{\nu}^2/4 + k^2V_0^2(1 - V_0^2/V_n^2) \right]^{1/2} \quad (\text{A14})$$

From (A14) we can see that the analytical growth rate is

$$\gamma = -\tilde{\nu}/2 \pm kv_0 \left(1 - v_0^2/v_n^2\right)^{1/2}, \quad kv_0 > \tilde{\nu} \quad (\text{A15})$$

and

$$\gamma = -\tilde{\nu} \left[1 + k^2 v_0^2 \left(1 - v_0^2/v_n^2\right) / \tilde{\nu}^2\right], \quad kv_0 < \tilde{\nu} \quad (\text{A16})$$

APPENDIX B

In this appendix we examine, analytically, the nonlinear evolution, to lowest order, of the Kelvin-Helmholtz instability with and without Pedersen coupling effects. The equations of motion, Eq. (10) (11) can be written

$$\frac{\partial N}{\partial t} + \frac{c}{B} \hat{e}_z \times \nabla \phi \cdot \nabla N = 0 \quad (B1)$$

$$\begin{aligned} \nabla \cdot \left\{ N \left[\frac{\partial \hat{c}}{\partial t} + \frac{c}{B} \left(\hat{c}_z \times \nabla \right) \cdot \nabla \hat{c} \right] \right\} &= 0 \\ &= - \nabla \cdot \left\{ \tilde{\nabla} N \left[\nabla \phi - \frac{B}{c} V_n \times \hat{e}_z \right] \right\} \end{aligned} \quad (B2)$$

Separating $\phi = \phi_0(y) + \delta\phi_{kx}(y) \exp [i(k_x x - \omega t)]$, $N = N_0(y) + \delta n_{kx}(y) \exp [i(k_x x - \omega t)]$, assuming approximate saturation in the nonlinear regime, i.e., $\partial/\partial t < \tilde{v}$ (B1) can be solved for δn_{kx} in terms of $\delta\phi_{kx}$. The result is inserted into (B2) giving, to lowest nonlinear order,

$$\frac{\partial \delta\phi_{kx}}{\partial t} + L(\delta\phi_{kx}) = \frac{1}{2} \sum_{\substack{k'_x + k''_x = k_x \\ \omega' + \omega'' = \omega}} \frac{V}{E_z \omega, k'_x \omega', k''_x \omega''} \frac{\delta\phi_{k'_x} \delta\phi_{k''_x}}{E_x k'_x k''_x} \quad (B3)$$

with

$$\begin{aligned} L(\delta\phi_{kx}) &= \frac{c}{B} \left[\frac{\partial}{\partial t} + \frac{c}{B} \left(\hat{c}_z \times \nabla \right) \cdot \nabla \right] \delta\phi_{kx} \\ &+ \frac{1}{2} \sum_{\substack{k'_x + k''_x = k_x \\ \omega' + \omega'' = \omega}} \frac{V}{E_z \omega, k'_x \omega', k''_x \omega''} \frac{\delta\phi_{k'_x} \delta\phi_{k''_x}}{E_x k'_x k''_x} \end{aligned}$$

where $L(\delta\phi)$ represents terms linear in $\delta\phi$. The expression for V represents the nonlinear interactions between modes \underline{k}' and \underline{k}'' such that $\underline{k}' + \underline{k}'' = \underline{k}$. The first two terms in the expression for V give the approximate wave coupling proportional to $\hat{\underline{k}} \times \underline{k}'' \cdot \underline{k}'$ when $\tilde{\nu} = 0.00$. This term vanishes if $\underline{k}' = k_x'' \hat{\underline{x}}$ and $\underline{k}'' = k_x' \hat{\underline{x}}$. As a result, in this lowest order approximation for nonlinear coupling, the mode-mode interactions along the k_x direction is enhanced when $\nu > 0$ since its coupling coefficient $\propto \underline{k}'' \cdot \underline{k}' \neq 0$ if $\underline{k}_x'' = k_x'' \hat{\underline{x}}$ and $\underline{k}' = k_x' \hat{\underline{x}}$. Furthermore, this coupling ($\tilde{\nu} > 0$) has $V \propto k^3$ and, thus, favors higher wavenumbers. This is consistent with the spectral results computed in Sections 4 and 5 which indicated small scale (high k) structure generation when $\tilde{\nu} > 0$ in the nonlinear regime.

TABLE 1

Spectral Indices of Transverse Averaged Power Spectra of
Potential and Density in Kelvin-Helmholtz Instability

	$\nu = 0$	$\nu = 0.1$	$\nu = 0.34$
$\delta\phi$ $P(k_x)$	5.4 ± 0.4	4.7 ± 0.2	4.6 ± 0.2
ϕ $P(k_x)$	5.4 ± 0.4	4.7 ± 0.2	4.6 ± 0.2
$\delta\phi$ $P(k_y)$	5.3 ± 0.3	5.3 ± 0.2	5.3 ± 0.2
ϕ $P(k_y)$	5.4 ± 0.4	5.2 ± 0.2	5.2 ± 0.2
δN $P(k_x)$	2.2 ± 0.2	1.9 ± 0.2	2.1 ± 0.2
N $P(k_x)$	2.2 ± 0.2	1.9 ± 0.2	2.1 ± 0.2
δN $P(k_y)$	2.3 ± 0.3	1.6 ± 0.2	1.7 ± 0.2
N $P(k_y)$	2.2 ± 0.3	1.8 ± 0.2	1.8 ± 0.2

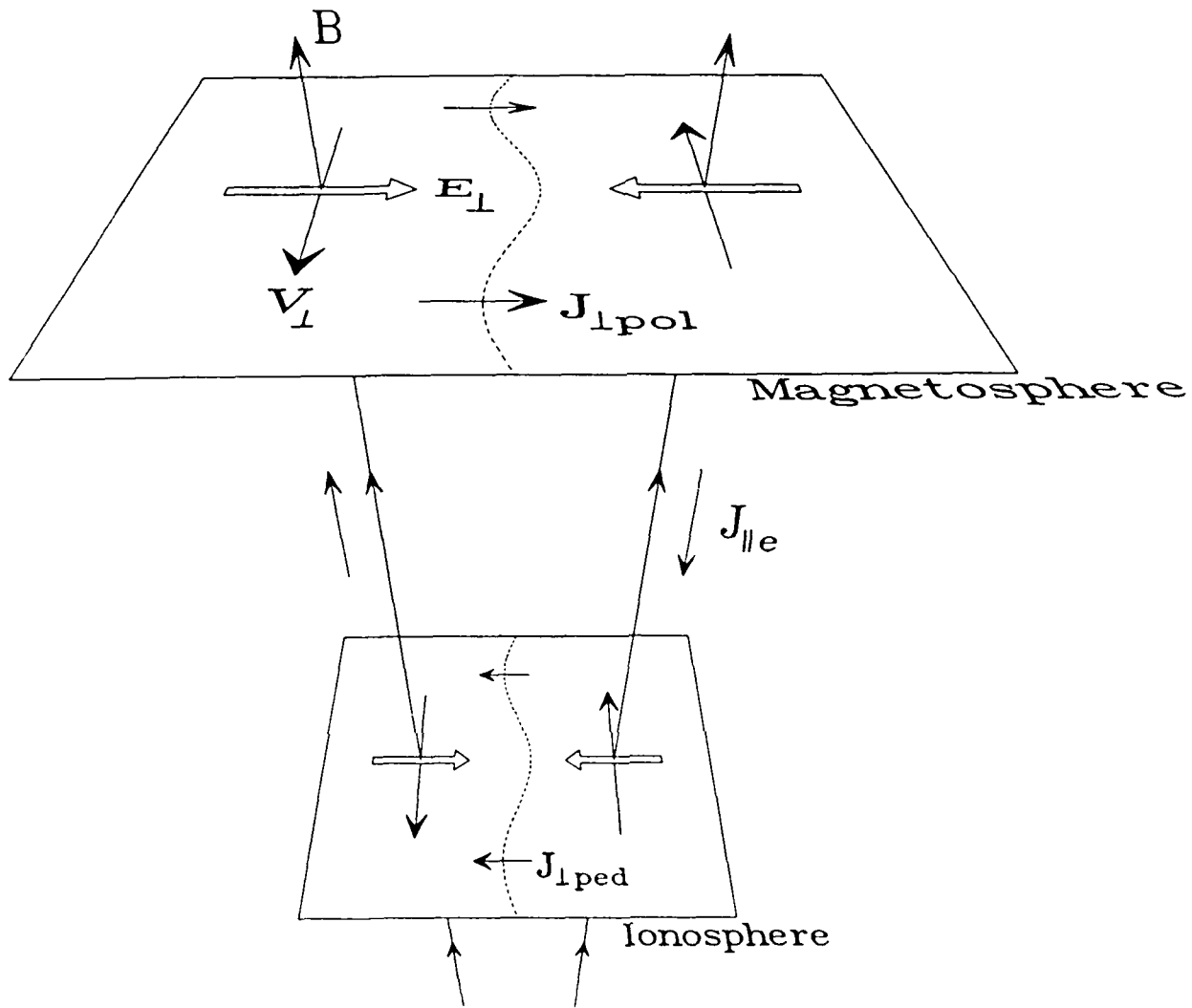


Fig. 1 — A diagram of the Kelvin-Helmholtz shear configuration in the presence of magnetosphere-ionosphere coupling. The dashed line represents the unstable shear interface, and the instability-driven currents are indicated: the perpendicular ion polarization and Pedersen currents in the magnetosphere and ionosphere respectively and the electron closing current parallel to the magnetic field.

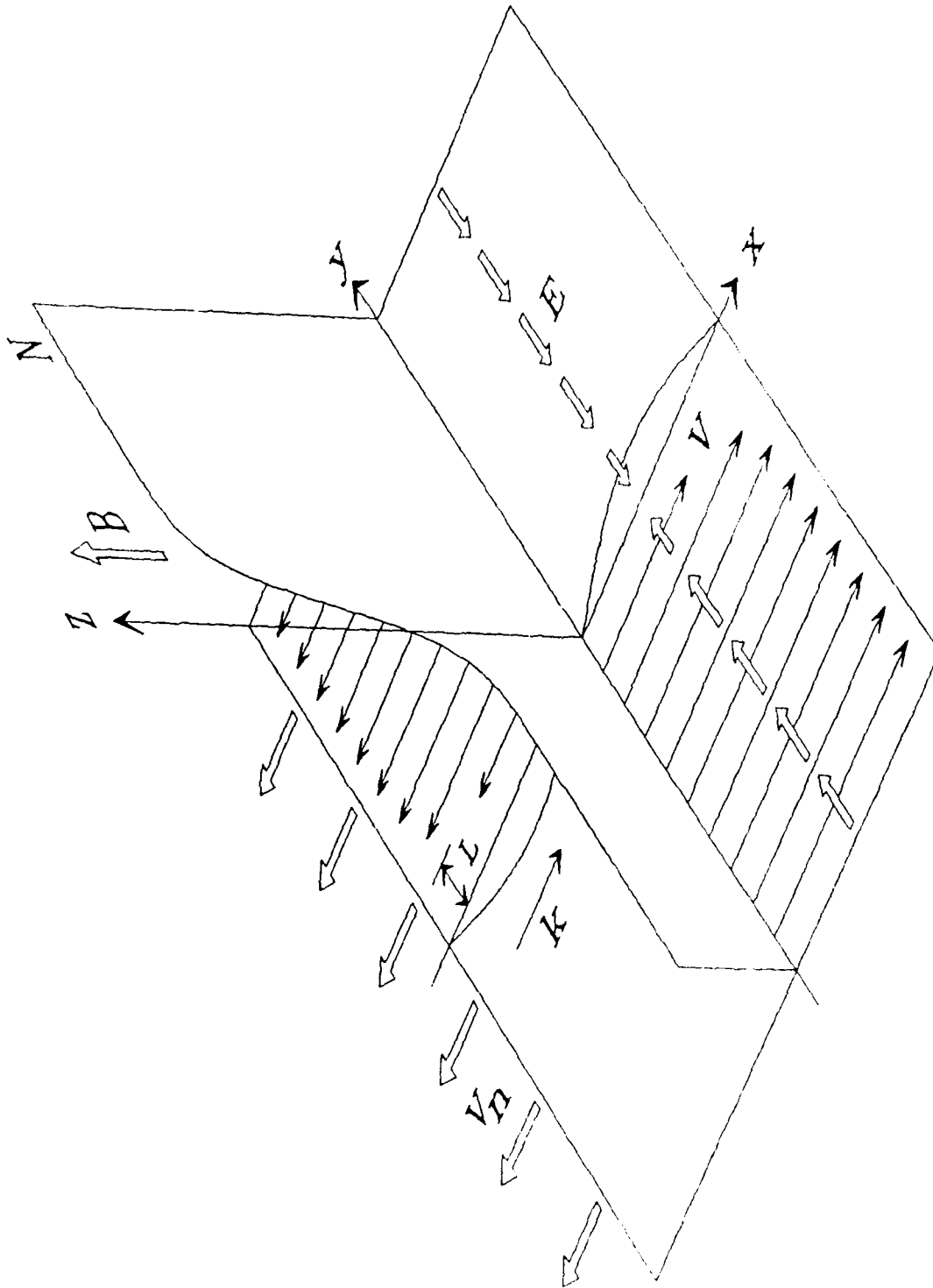


Fig. 2 - The configuration of the simulation model, indicating the velocities and electric fields along with profiles of the velocity shear and density gradient relative to the scale length L and the unstable wave vector k .

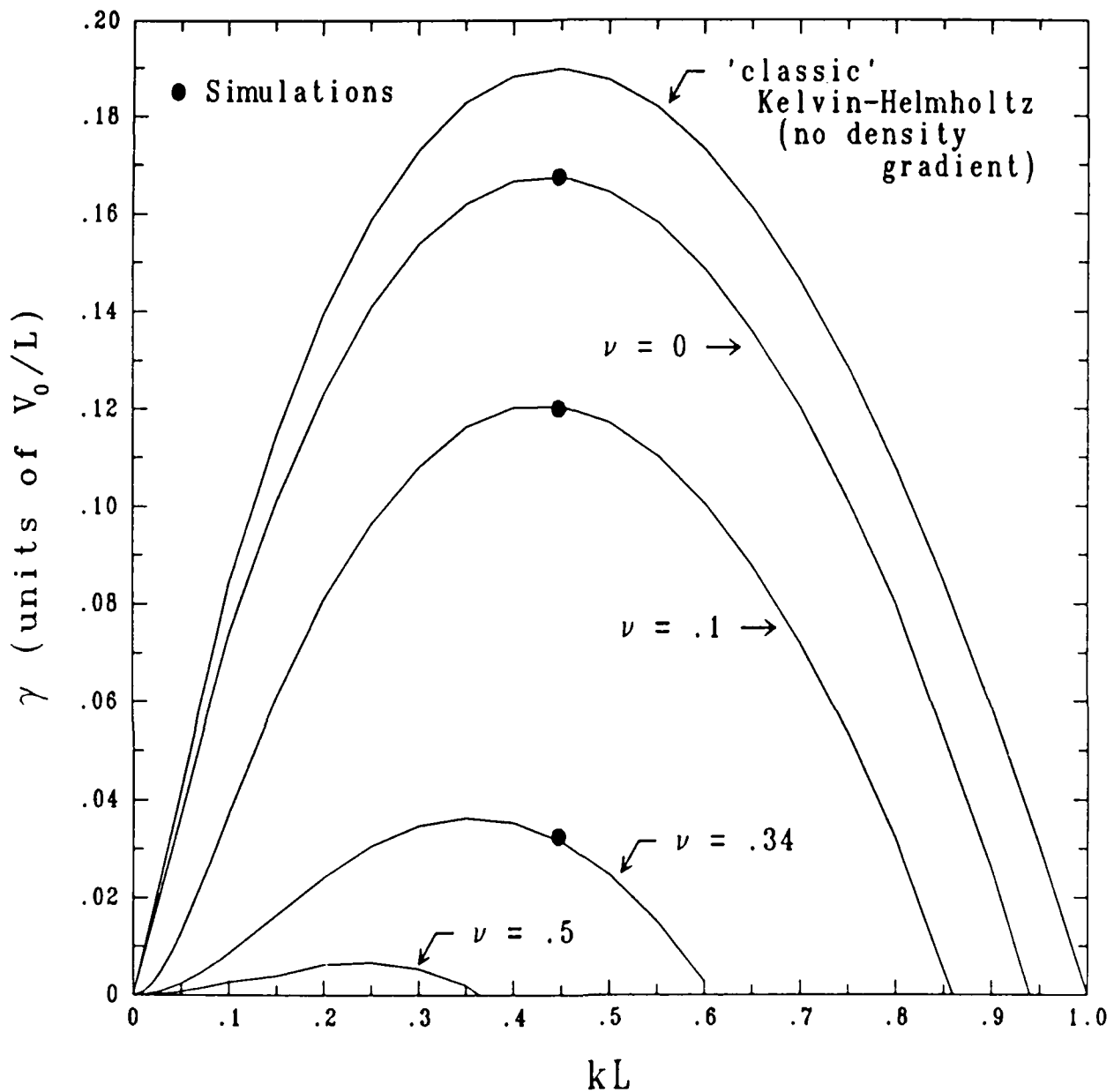


Fig. 3 — The linear growth rates of the Kelvin-Helmholtz instability versus wave number k for the 'classic' (no density gradient) case and for four collisional cases ($\nu = 0.0, 0.10, 0.34, 0.50$) with a density jump of 3:1. The bullets mark the three simulation cases.

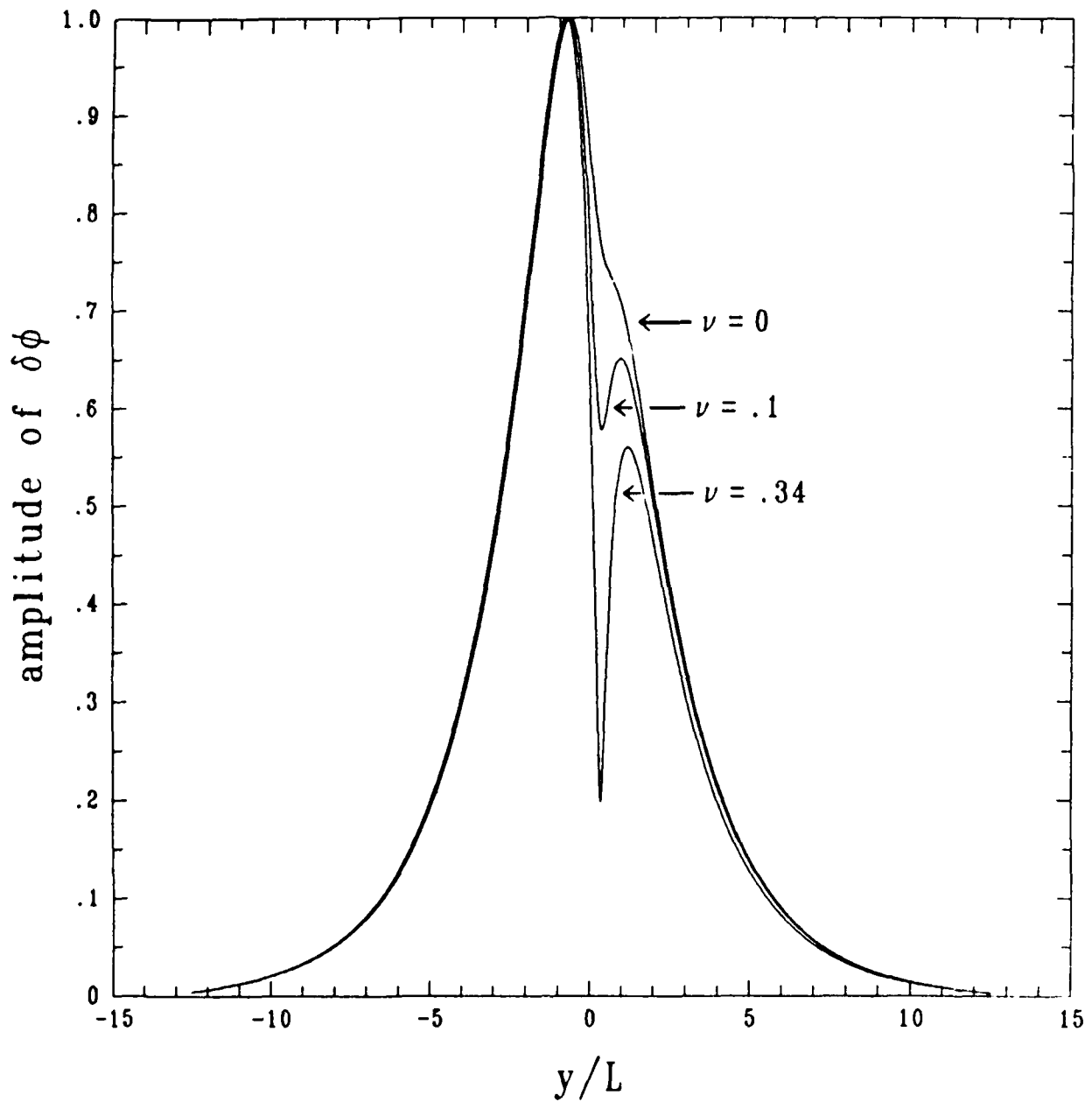


Fig. 4 -- Eigenfunction plots for the three simulation cases. a) The amplitudes of the Fourier components $\delta\phi$ versus y . b) The phases of the Fourier components $\delta\phi$ versus y . c) Contour plots of the complete 2-dimensional eigenfunctions. Dashed lines represent negative contours.

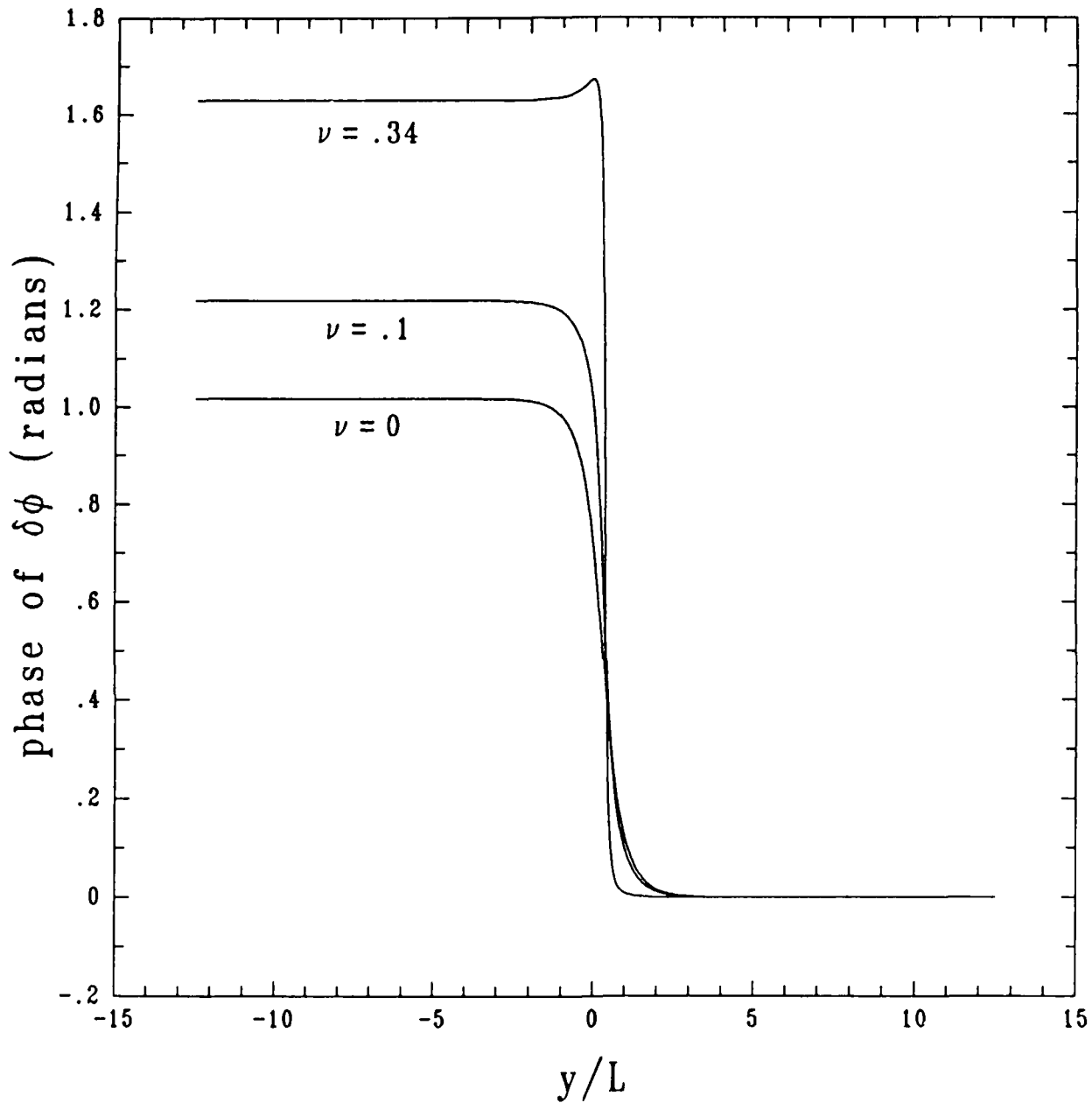


Fig. 4 (Cont'd) — Eigenfunction plots for the three simulation cases. a) The amplitudes of the Fourier components $\delta\phi$ versus y . b) The phases of the Fourier components $\delta\phi$ versus y . c) Contour plots of the complete 2-dimensional eigenfunctions. Dashed lines represent negative contours.

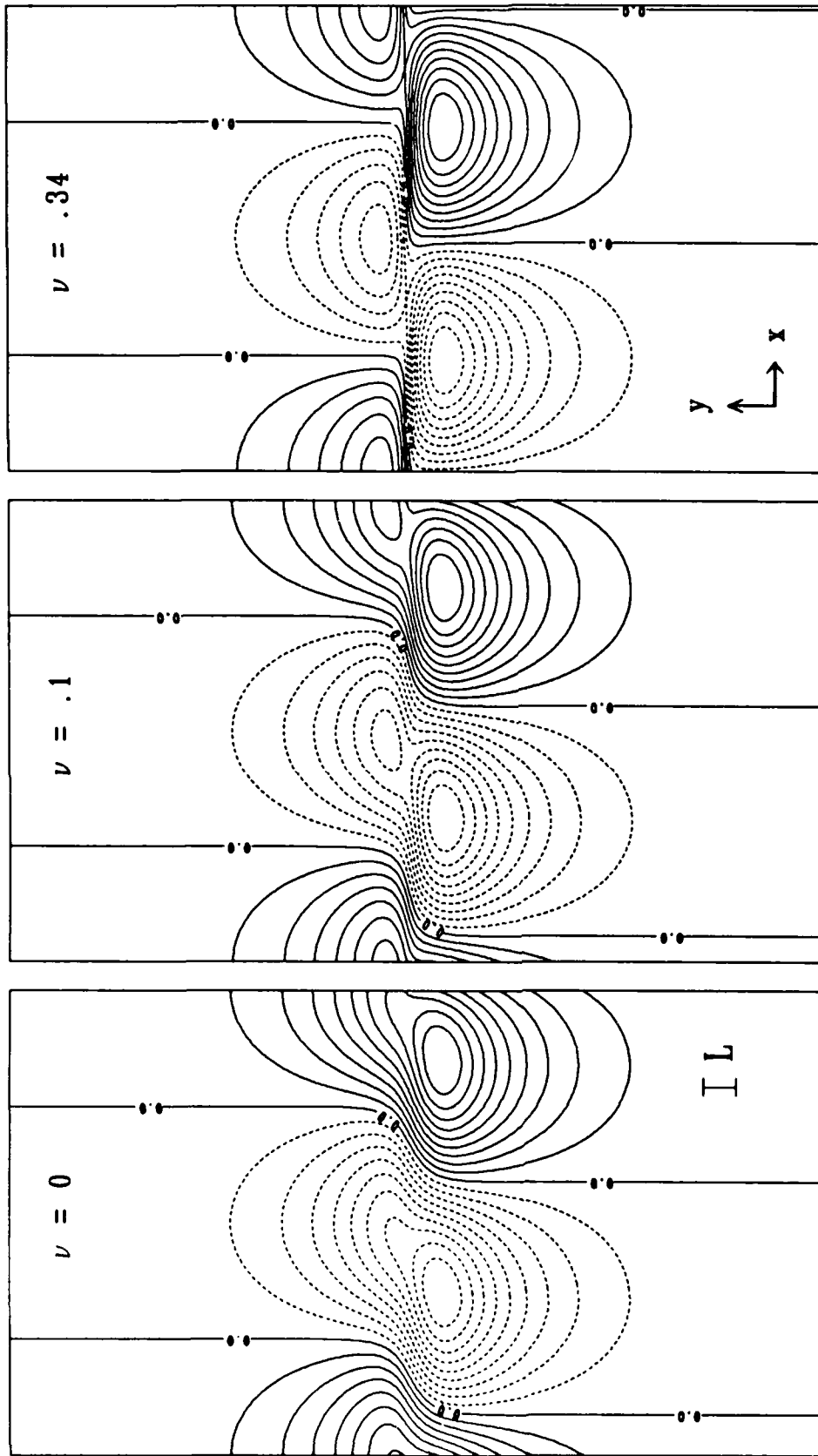


Fig. 4 (Cont'd) — Eigenfunction plots for the three simulation cases. a) The amplitudes of the Fourier components $\delta\phi$ versus y . b) The phases of the Fourier components $\delta\phi$ versus y . c) Contour plots of the complete 2-dimensional eigenfunctions. Dashed lines represent negative contours.

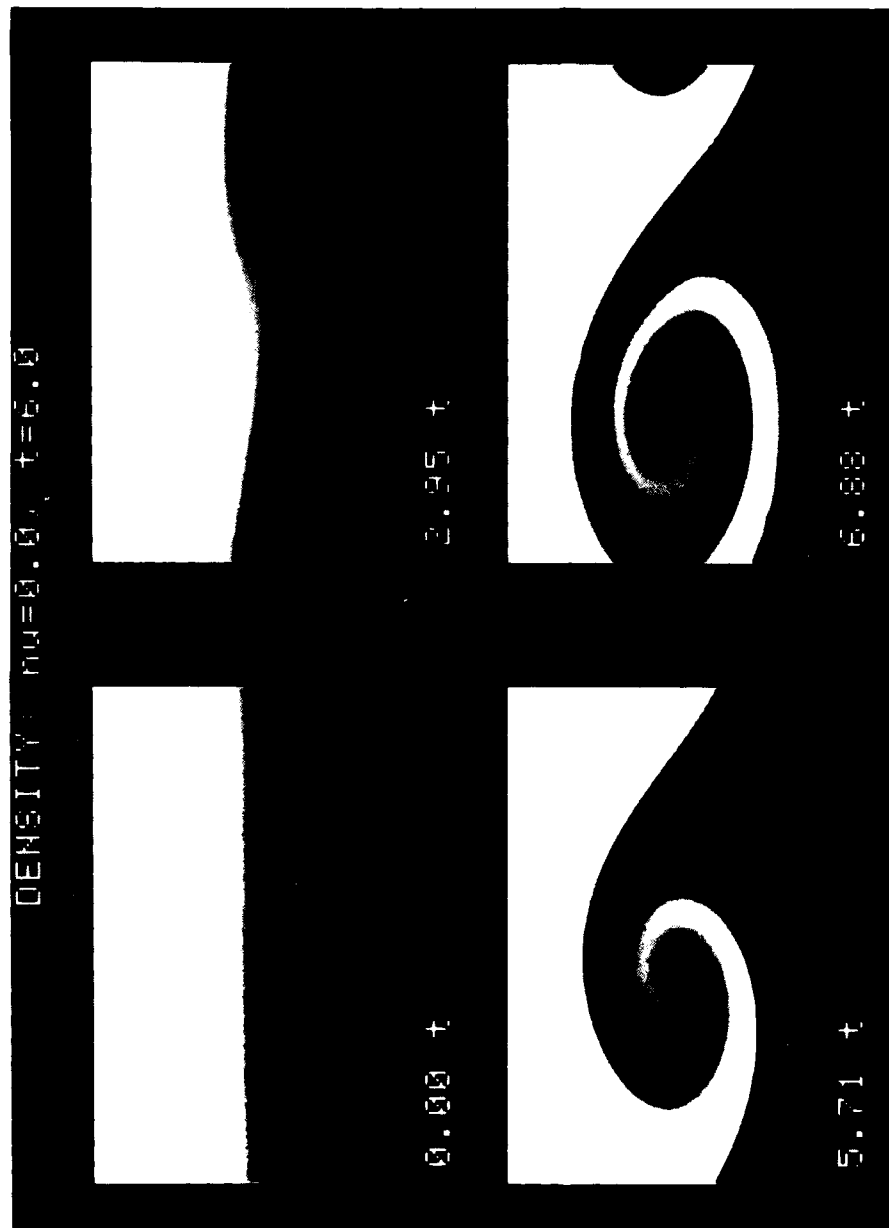


Fig. 5 — Results of the $\nu = 0.00$ simulation at four times: 0.00t, 2.95t, 5.71t, 6.88t where $t = v^{-1} = 6.0 L/V_0$. a) Density. b) Potential contours.

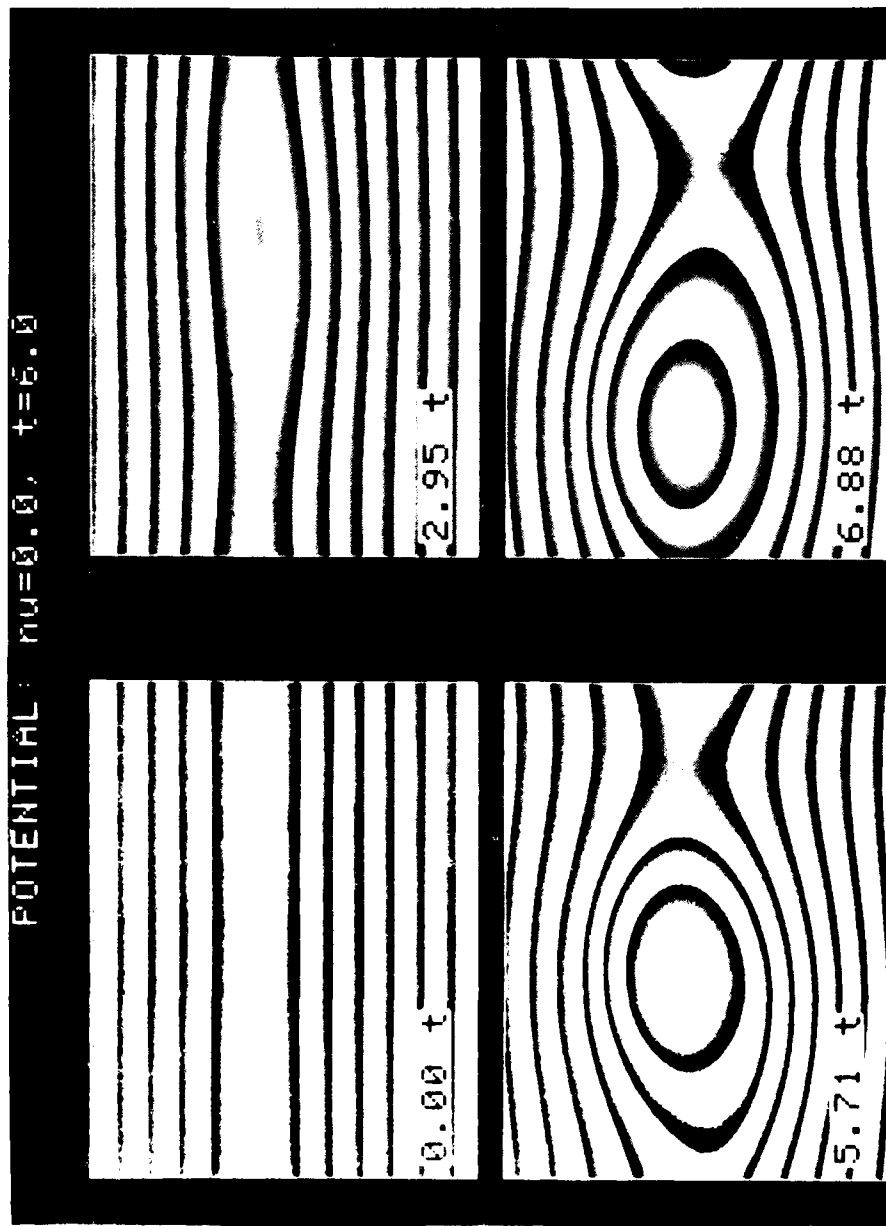


Fig. 5 (Cont'd) — Results of the $\nu = 0.00$ simulation at four times: 0.00t, 2.95t, 5.71t, 6.88t where $t = \nu^{-1} = 6.0 L/V_0$. a) Density. b) Potential contours.

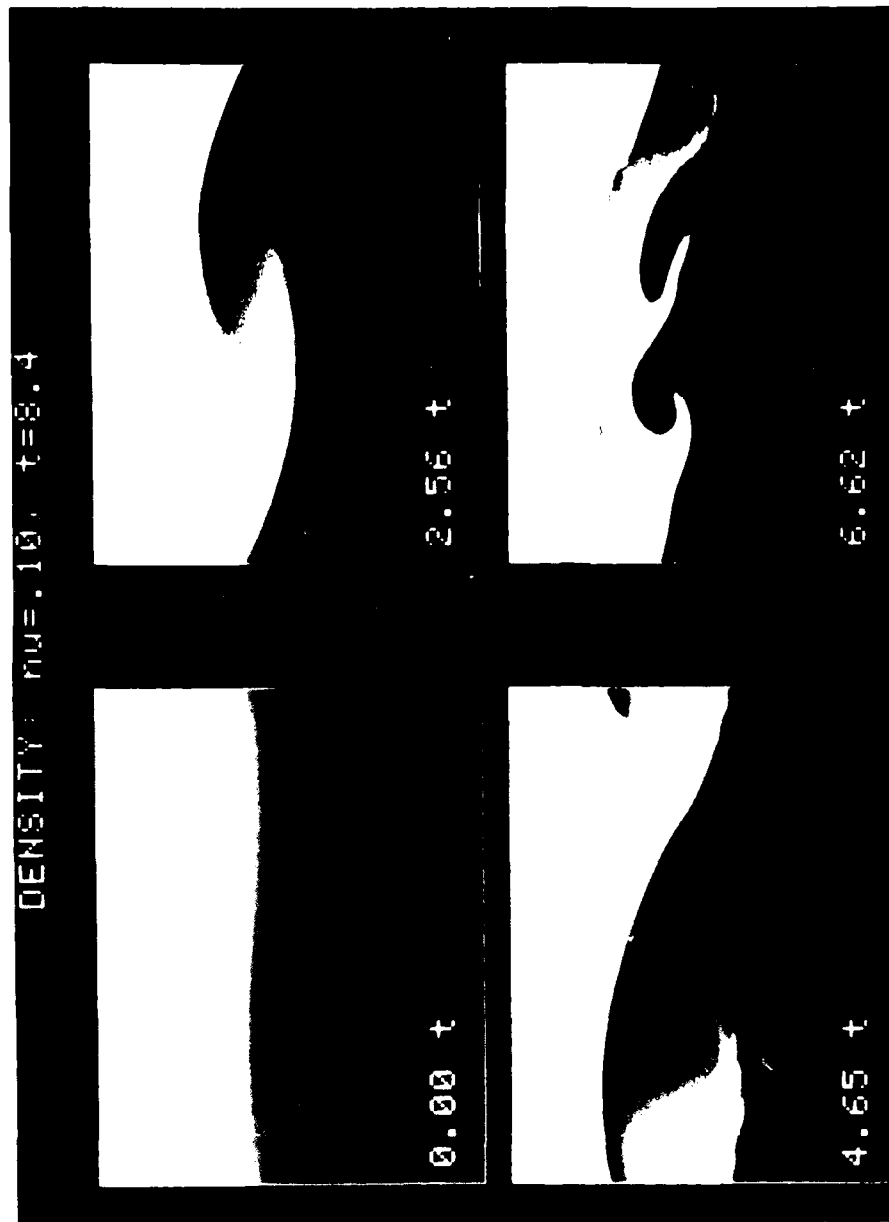


Fig. 6 — Results of the $\nu = 0.10$ simulation at four times: 0.00t, 2.56t, 4.65t, 6.62t where $t = \nu^{-1} = 8.4 L/V_0$. a) Density. b) Potential contours.

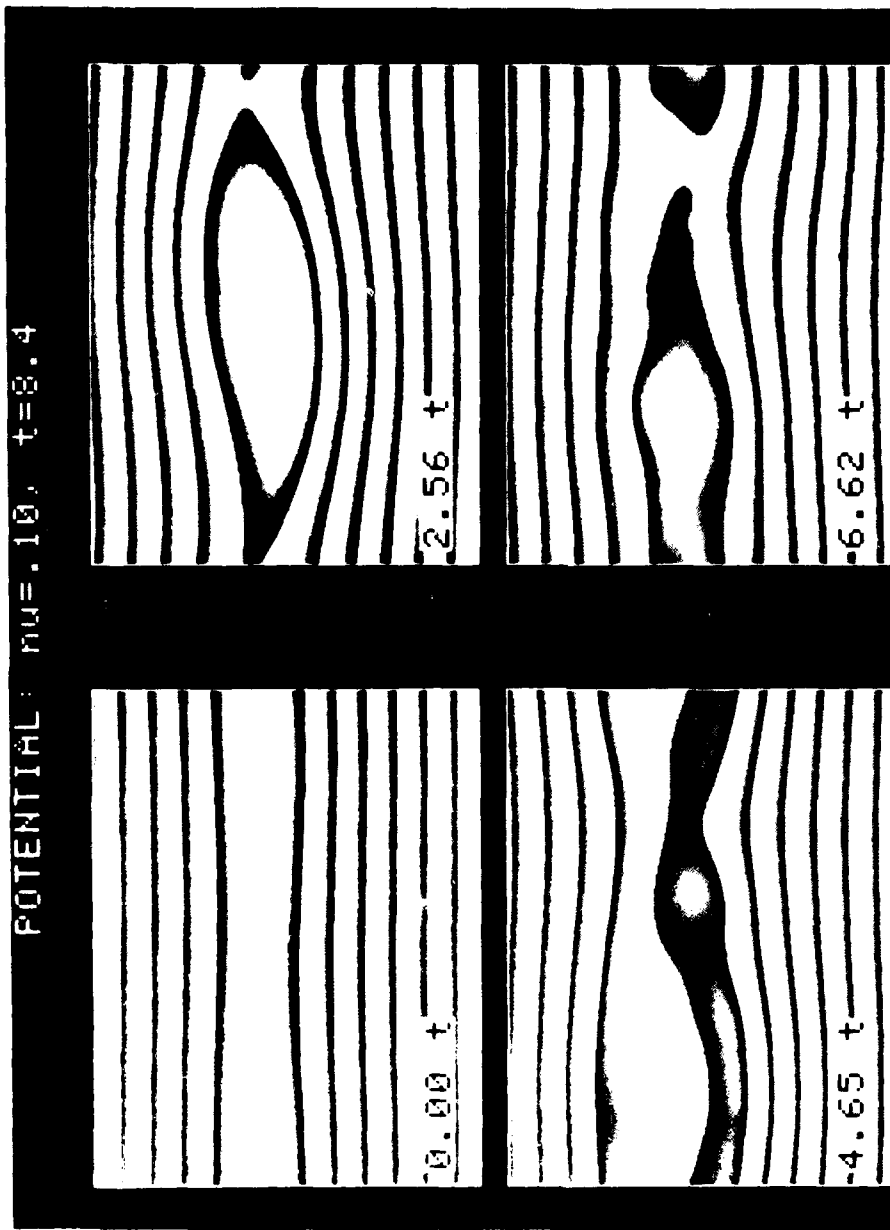


Fig. 6 (Cont'd) — Results of the $\nu = 0.10$ simulation at four times: 0.00t, 2.56t, 4.65t, 6.62t where $t = \nu^{-1} = 8.4 L/V_0$. a) Density. b) Potential contours.

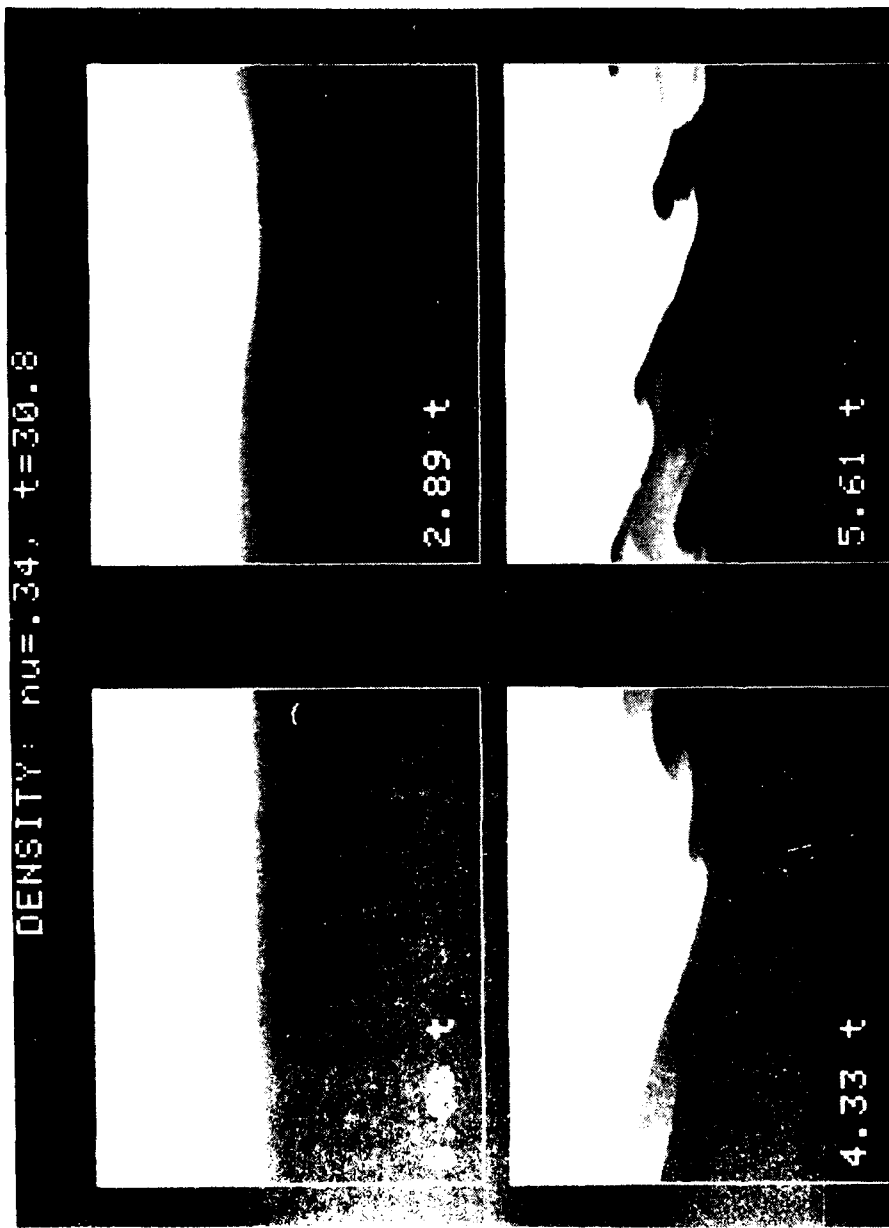


Fig. 7 — Results of the $\nu = 0.34$ simulation at four times: 0.00t, 2.89t, 4.33t, 5.61t where $t = v^{-1} = 30.8 L/V_0$. a) Density. b) Potential contours.

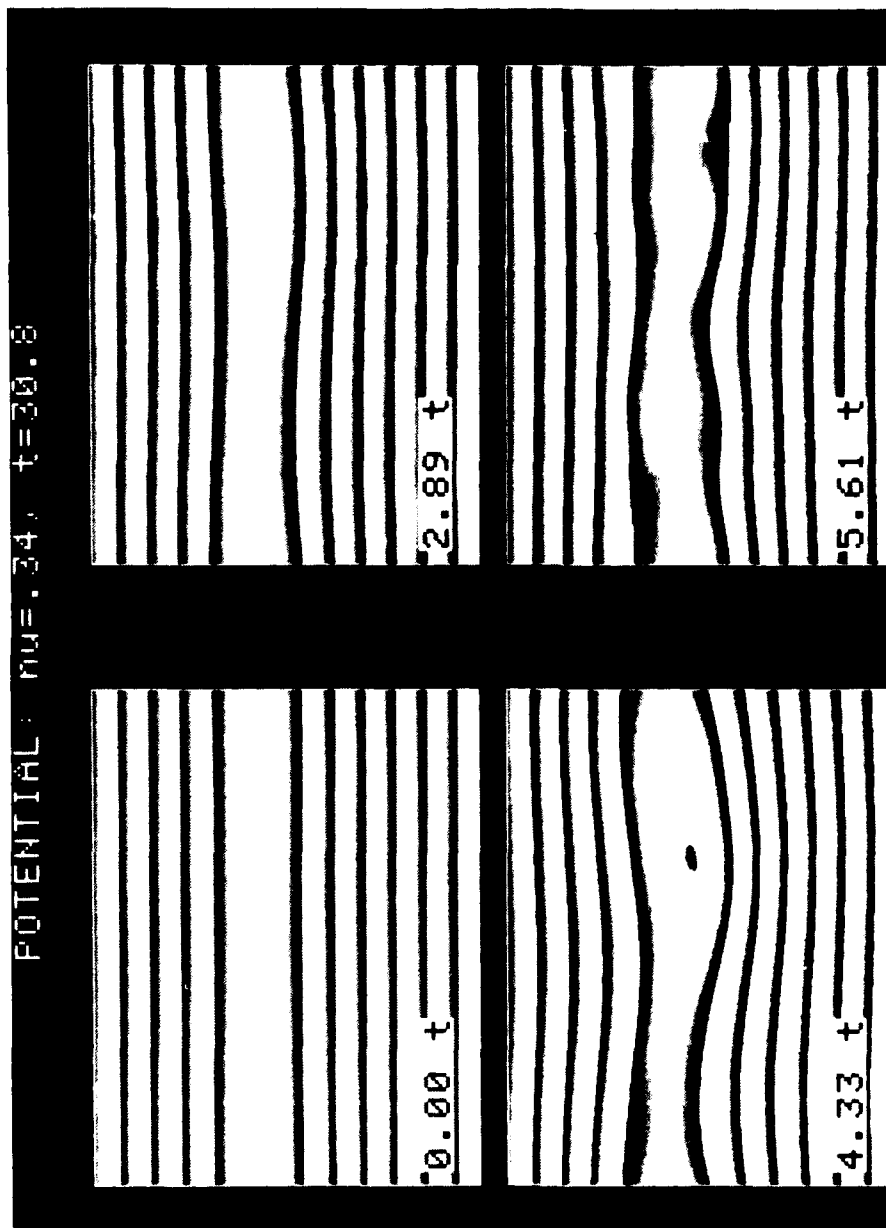


Fig. 7 (Cont'd) — Results of the $\nu = 0.34$ simulation at four times: 0.00t, 2.89t, 4.33t, 5.61t where $t = \nu^{-1} = 30.8 L/V_0$. a) Density. b) Potential contours.

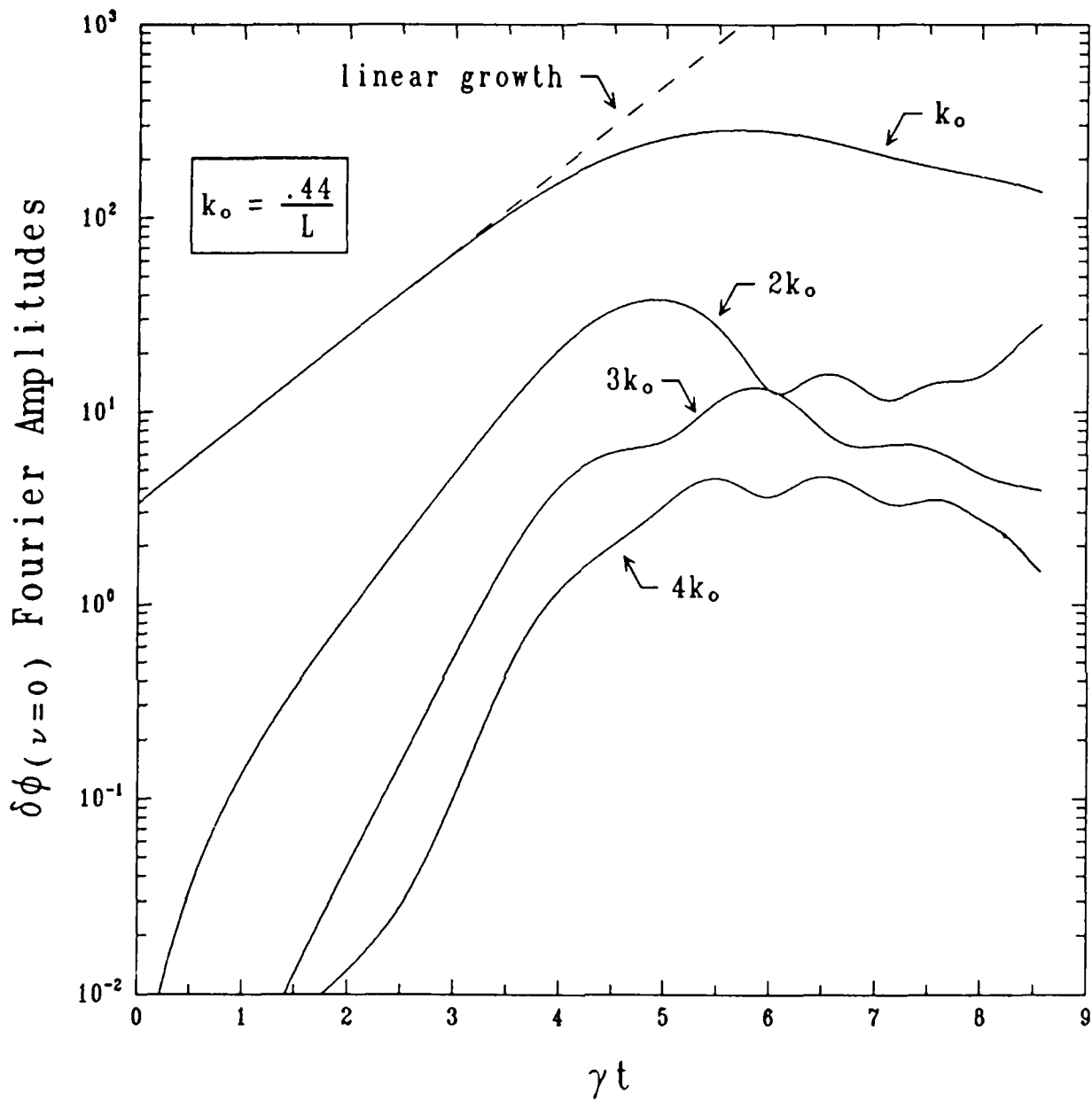


Fig. 8 -- Plot of amplitudes of the four most significant Fourier components of the potential $|\phi_{kx}(t)|$ vs. γt for the $\nu = 0.00$ case.

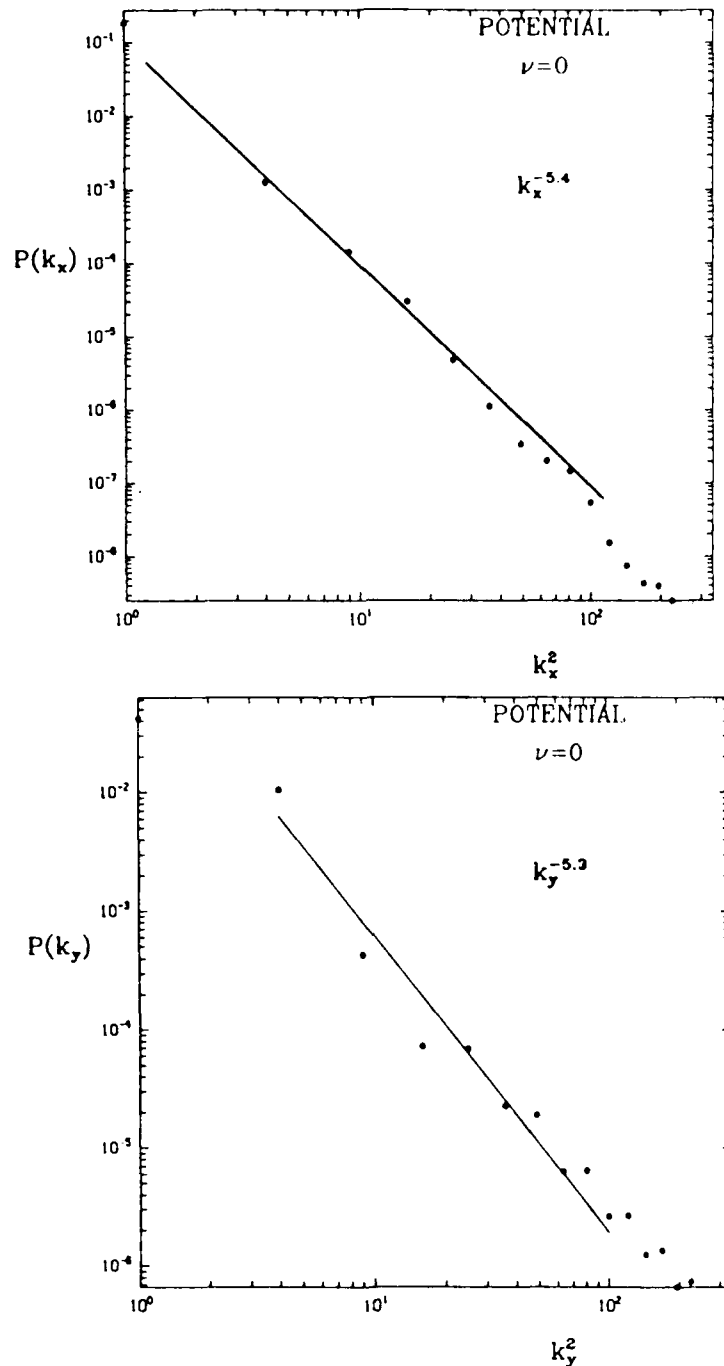


Fig. 9 - Plot of the time and transverse averaged power spectra (a) $P(k_x)$ and (b) $P(k_y)$ for $\delta\phi$ for $\nu = 0.00$. The wavenumbers k_x and k_y are in units of $k_{0x} = 2\pi/L_x \approx 0.5/L$ and $k_{0y} = 2\pi/L_y \approx 1.6/L$, respectively, where L_x is the length of the system in the x direction, L_y is the system length in the uniform mesh region in the y -direction, and L is the width of the shear layer. Typically, $L \sim 1 - 10$ km so that $k_{0x} \approx 0.50 - 0.05 \text{ km}^{-1}$ and $k_{0y} \approx 1.60 - 0.16 \text{ km}^{-1}$.

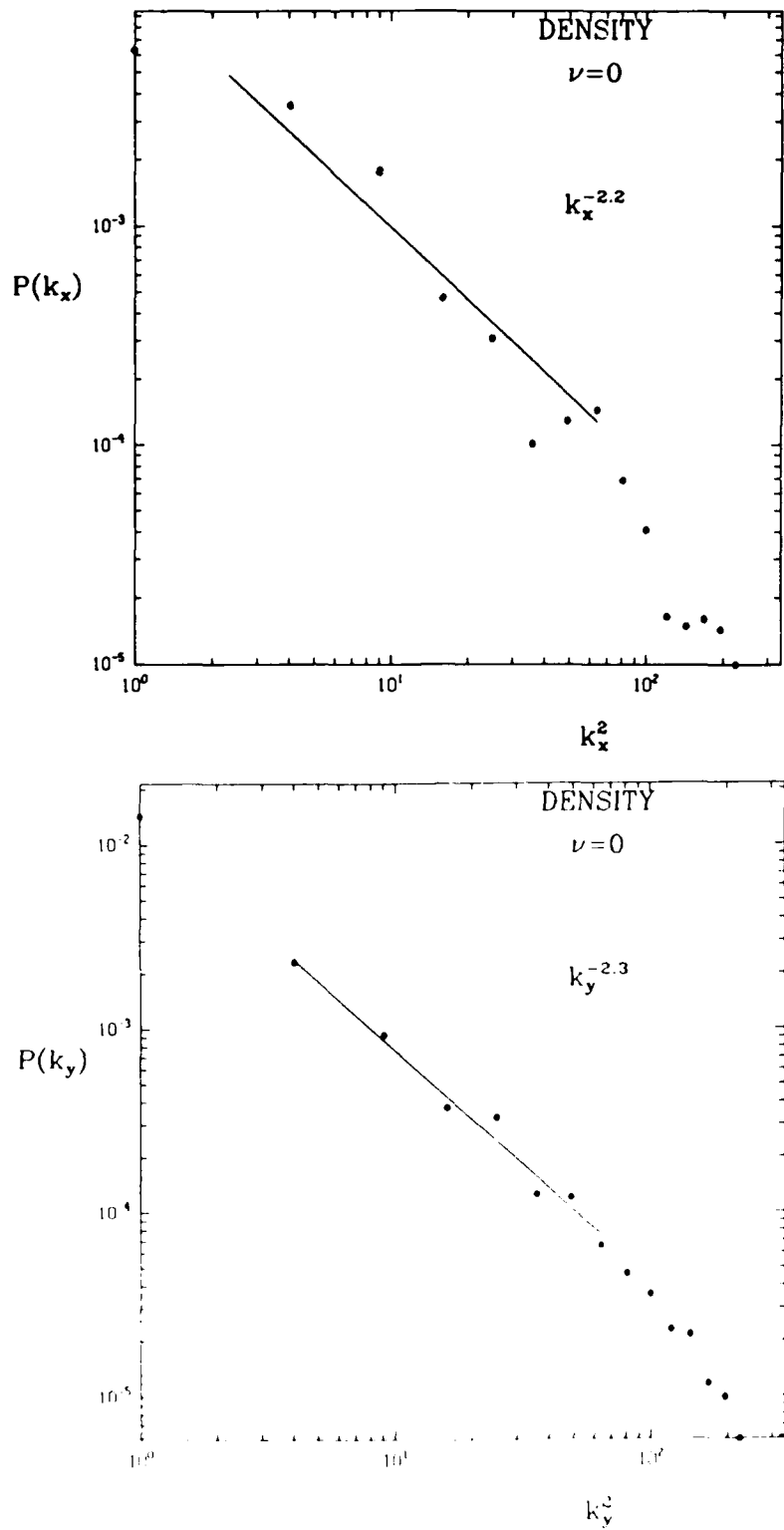


Fig. 10 — Plot of the time and transverse averaged power spectra (a) $P(k_x)$ and (b) $P(k_y)$ for δN for $\nu = 0.00$. The units are described in Fig. 9.

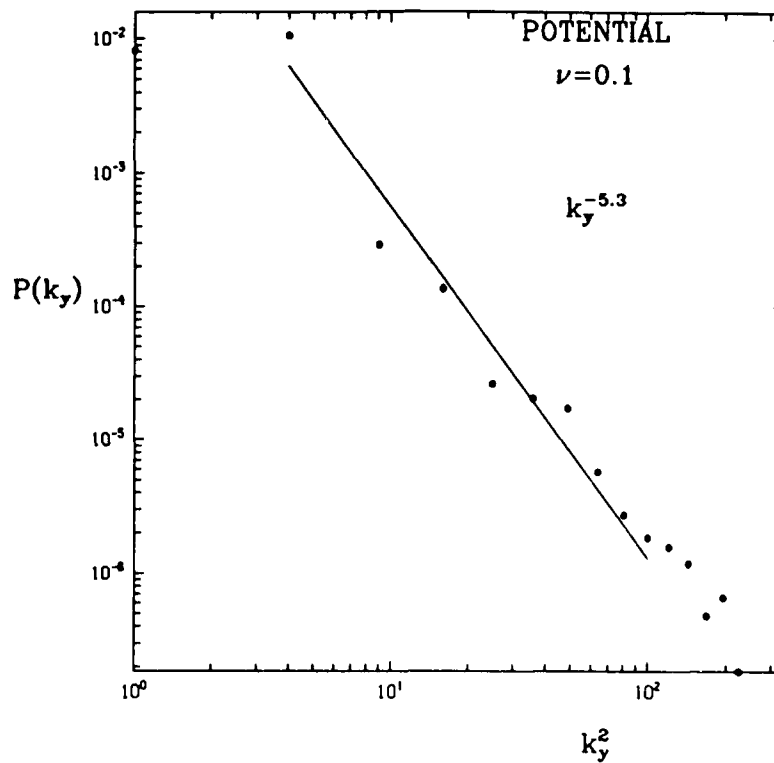
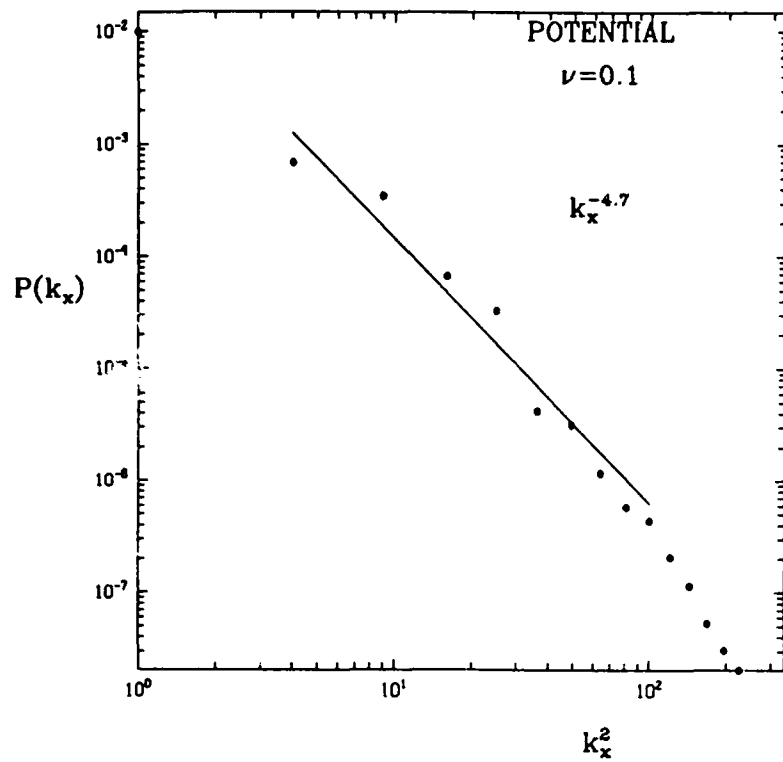


Fig. 11 — Plot of the time and transverse averaged power spectra (a) $P(k_x)$ and (b) $P(k_y)$ for $\delta\phi$ for $\nu = 0.10$. The units are described in Fig. 9.

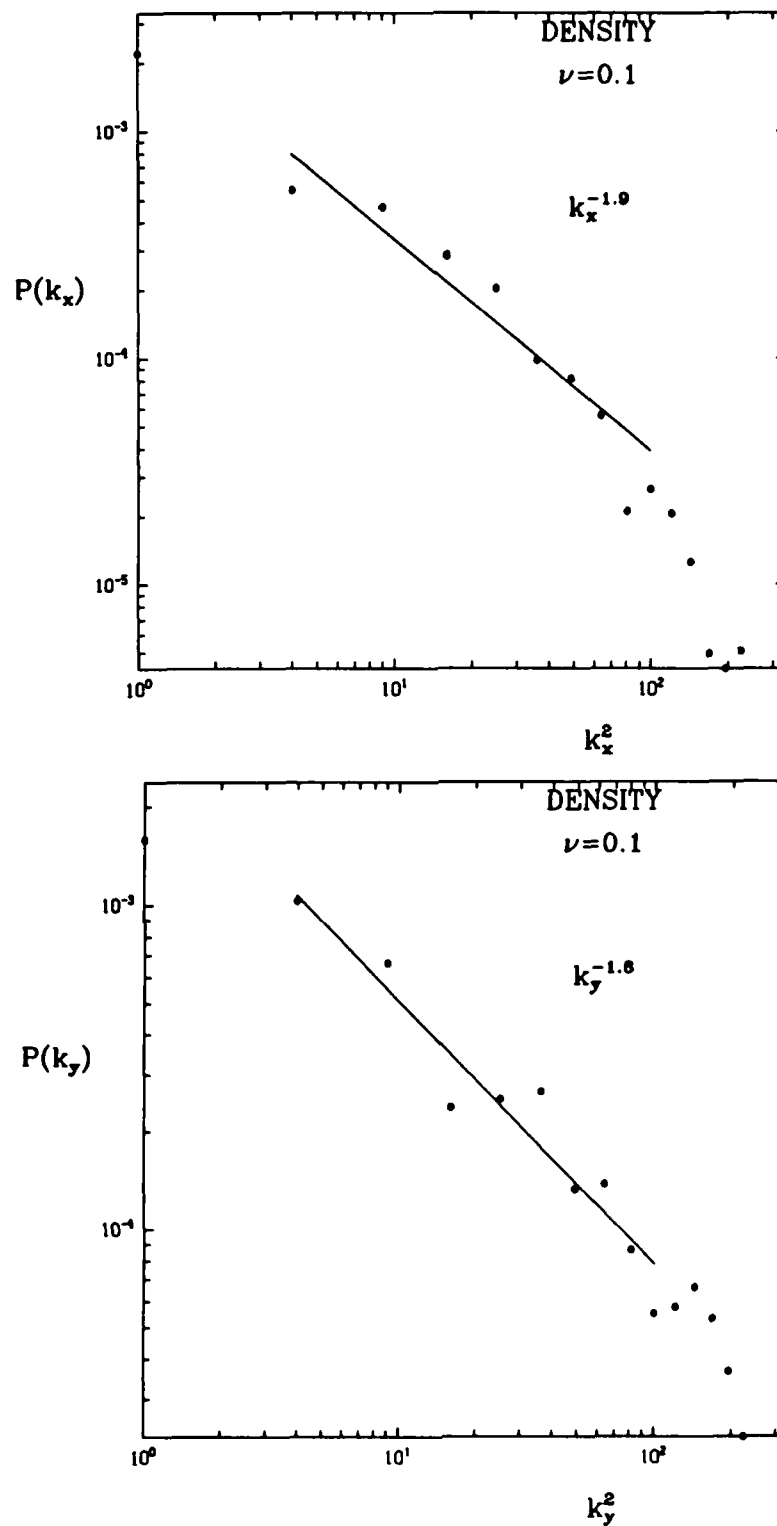


Fig. 12 — Plot of the time and transverse averaged power spectra (a) $P(k_x)$ and (b) $P(k_y)$ for δN for $\nu = 0.10$. The units are described in Fig. 9.

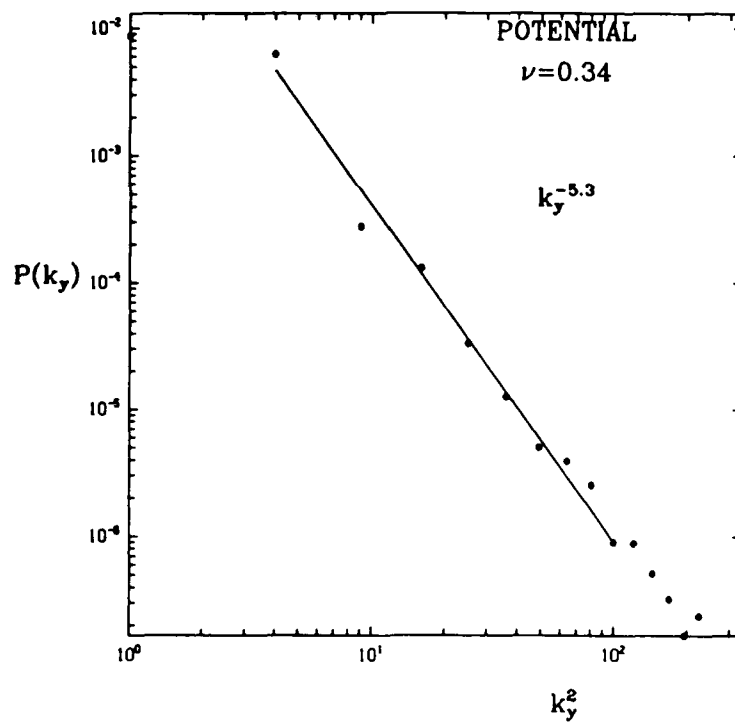
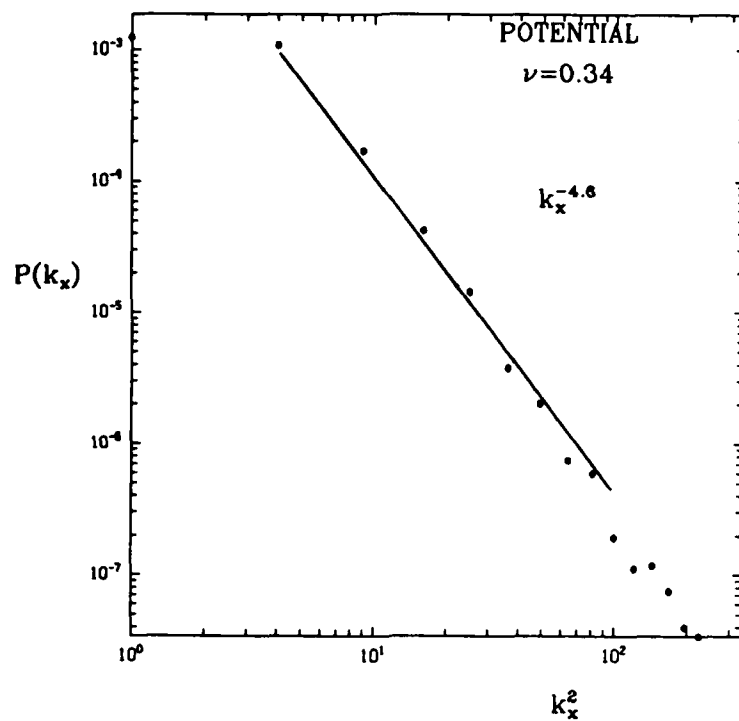


Fig. 13 — Plot of the time and transverse averaged power spectra (a) $P(k_x)$ and (b) $P(k_y)$ for $\delta\phi$ for $\nu = 0.34$. The units are described in Fig. 9.

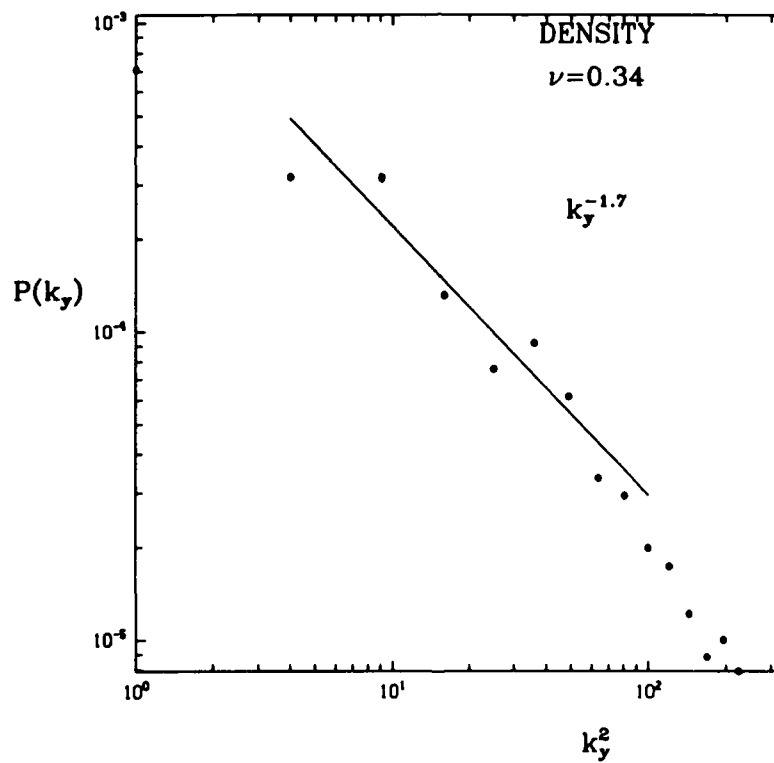
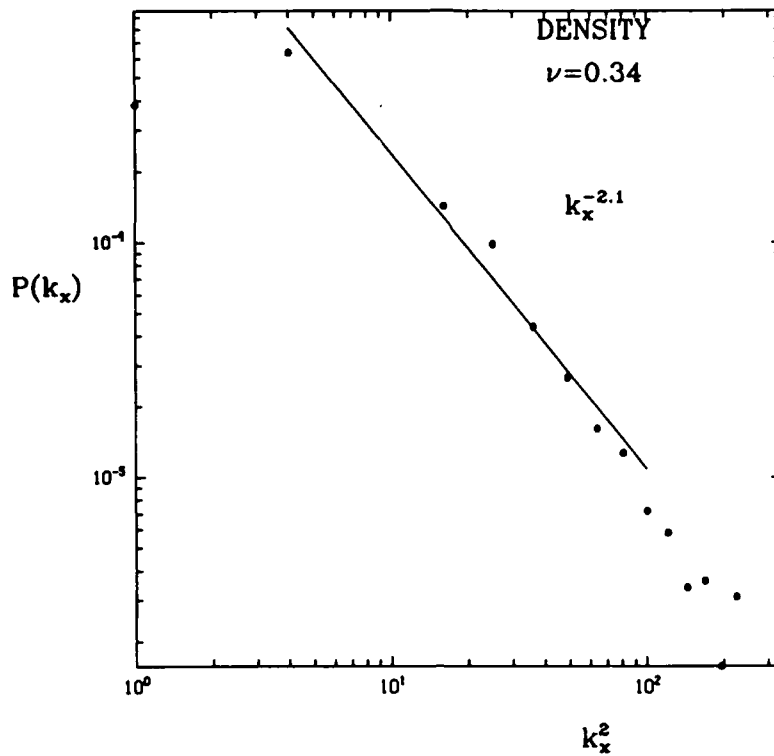


Fig. 14 — Plot of the time and transverse averaged power spectra (a) $P(k_x)$ and (b) $P(k_y)$ for δN for $\nu = 0.34$. The units are described in Fig. 9.

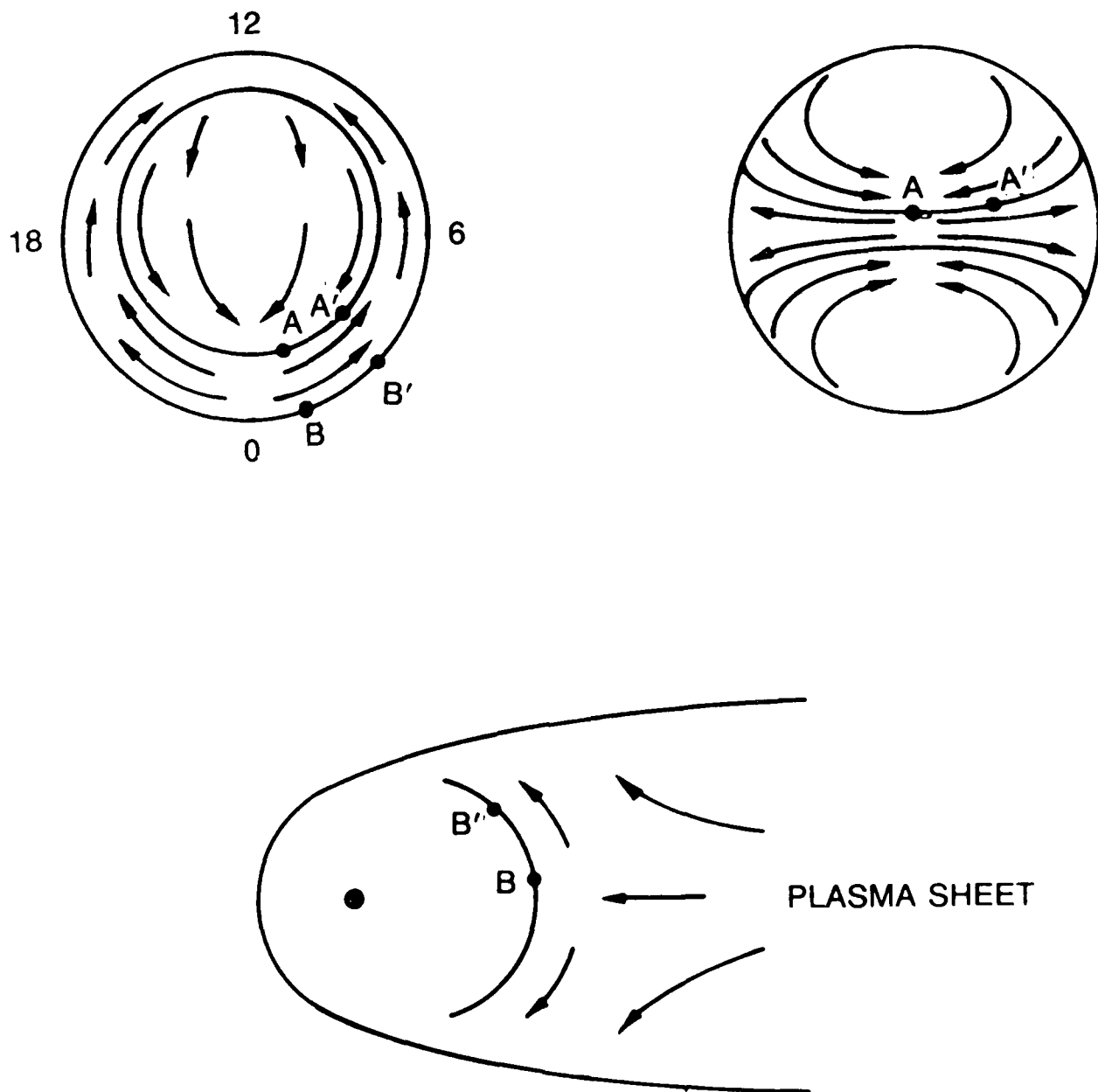


Fig. 15 — Sketch of regions of strong velocity shear in high latitude space plasma, showing the (a) polar ionosphere viewed from above, (b) magnetotail as viewed toward the sun, and (c) equatorial plane and plasma sheet of the magnetosphere.

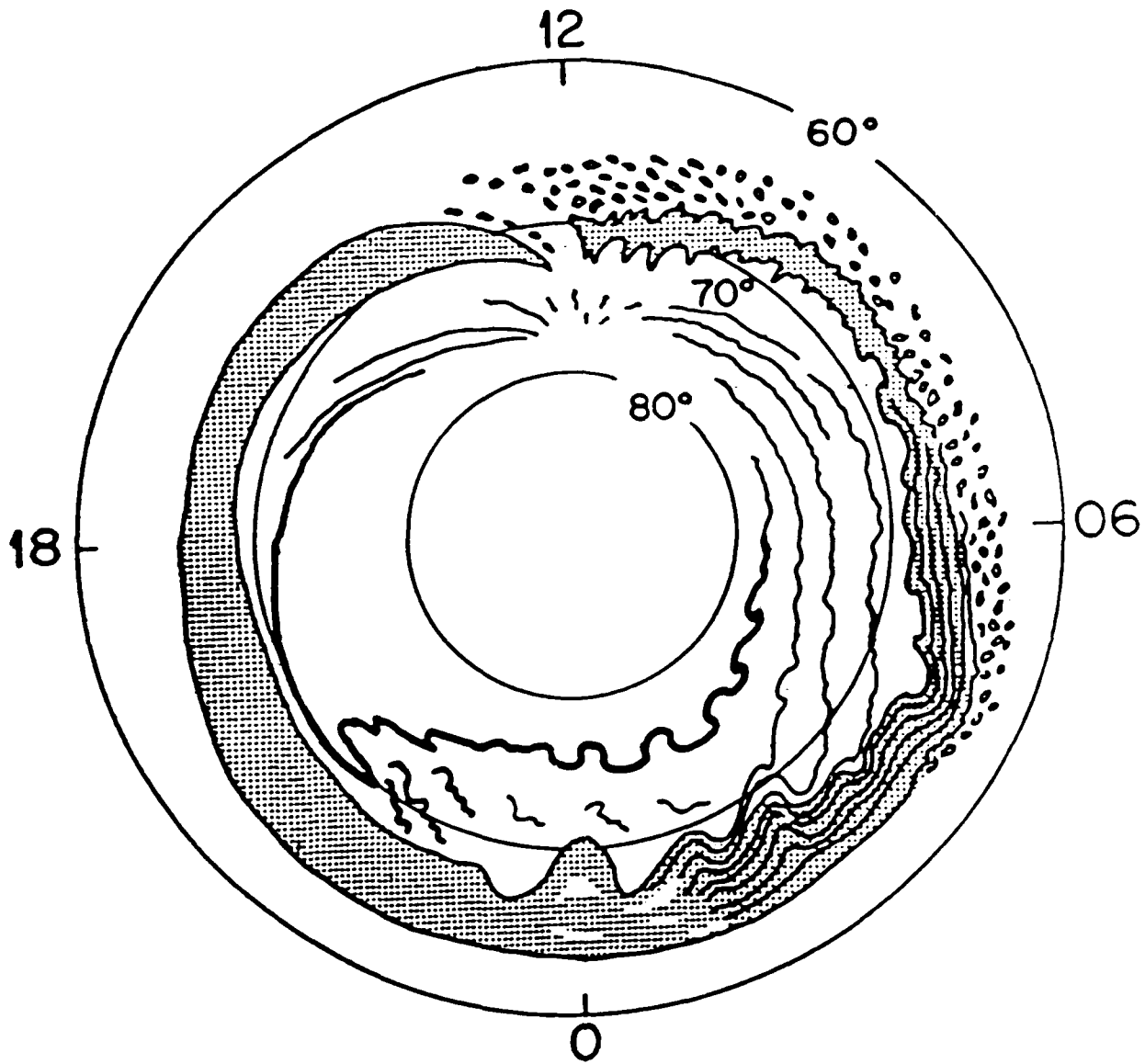


Fig. 16 — Sketch of auroral morphology [Akasofu, 1976].

DISTRIBUTION LIST

DEPARTMENT OF DEFENSE

ASSISTANT SECRETARY OF DEFENSE
COMM, COM, CONT 7 INTELL
WASHINGTON, DC 20301

DIRECTOR
COMMAND CONTROL TECHNICAL CENTER
PENTAGON 5M BE 685
WASHINGTON, DC 20301
01CY ATTN C-650
01CY ATTN C-312 R. MASON

DIRECTOR
DEFENSE ADVANCED RSCH PROG AGENCY
ARCHITECT BUILDING
1400 WILSON BLVD.
ARLINGTON, VA 22209
01CY ATTN NUCLEAR
MONITORING RESEARCH
01CY ATTN STRATEGIC TECH OFFICE

DEFENSE COMMUNICATION ENGINEER CENTER
1860 WIEHLE AVENUE
RESTON, VA 22090
01CY ATTN CODE R410
01CY ATTN CODE R812

DIRECTOR
DEFENSE NUCLEAR AGENCY
WASHINGTON, DC 20305
01CY ATTN STVL
01CY ATTN TITL
01CY ATTN DDST
01CY ATTN RAAF

COMMANDER
FIELD COMMAND
DEFENSE NUCLEAR AGENCY
KIRTLAND, AFB, NM 87115
01CY ATTN FCPR

DEFENSE NUCLEAR AGENCY
SAO/DNA
BUILDING 20674
KIRTLAND AFB, NM 87115
01CY ATTN D.C. THORNBURG

DIRECTOR
INTERSERVICE NUCLEAR WEAPNS CENTER
KIRTLAND AFB, NM 87115
01CY ATTN DOCUMENT CONTR L

JOINT PROGRAM MANAGEMENT OFFICE
WASHINGTON, DC 20330
01CY ATTN J-3 WWMCCS EVALUATION
OFFICE

DIRECTOR
JOINT STRAT TGT PLANNING STAFF
OFFUTT AFB
OMAHA, NB 68113
01CY ATTN JSTPS/JLKS
01CY ATTN JPST G. GOETZ

CHIEF
LIVERMORE DIVISION FLD COMMAND DNA
DEPARTMENT OF DEFENSE
LAWRENCE LIVERMORE LABORATORY
P.O. BOX 808
LIVERMORE, CA 94550
01CY ATTN FCPRL

COMMANDANT
NATO SCHOOL (SHAPE)
APO NEW YORK 09172
01CY ATTN U.S. DOCUMENTS OFFICER

UNDER SECY OF DEF FOR RPTG & EN -
DEPARTMENT OF DEFENSE
WASHINGTON, DC 20301
01CY ATTN STRATEGIC & SPACE
SYSTEMS (OS)

COMMANDER/DIRECTOR
ATMOSPHERIC SCIENCES LABORATORY
U.S. ARMY ELECTRONICS COMMAND
WHITE SANDS MISSILE RANGE, NM 88160
01CY ATTN DELAS-EO, P. NILES

DIRECTOR
RMD ADVANCED TECH CTR
HUNTSVILLE OFFICE
P.O. BOX 1500
HUNTSVILLE, AL 35897
01CY ATTN ATC-T MELVIN T. CASE
01CY ATTN ATC-D W. DAVID
01CY ATTN ATC-R DON BUCH

PROGRAM MANAGER
BMD PROGRAM OFFICE
5001 EISENHOWER AVENUE
ALEXANDRIA, VA 22333
O1CY ATTN DACS-BMT J. SHEA

CHIEF C-E SERVICES DIVISION
U.S. ARMY COMMUNICATIONS CMD
PENTAGON RM 1B269
WASHINGTON, DC 20310
O1CY ATTN C- E-SERVICES DIVISION

COMMANDER
U.S. ARMY COMM-ELEC ENGRG INSTAL AGY
FT. HUACHUCA, AZ 85613
O1CY ATTN CCC-EMEO GEORGE LANE

COMMANDER
U.S. ARMY FOREIGN SCIENCE & TECH CTR
220 7TH STREET, NE
CHARLOTTESVILLE, VA 22901
O1CY ATTN DRXST-SD

COMMANDER
U.S. ARMY MATERIAL DEV & READINESS CMD
5001 EISENHOWER AVENUE
ALEXANDRIA, VA 22333
O1CY ATTN DRCLDC J.A. BENDER

COMMANDER
U.S. ARMY NUCLEAR AND CHEMICAL AGENCY
7500 BACKLICK ROAD
BLDG 2073
SPRINGFIELD, VA 22150
O1CY ATTN LIBRARY

DIRECTOR
U.S. ARMY BALLISTIC RESEARCH
LABORATORY
ABERDEEN PROVING GROUND, MD 21005
O1CY ATTN TECH LIBRARY,
EDWARD BAICY

COMMANDER
U.S. ARMY SATCOM AGENCY
FT. MONMOUTH, NJ 07703
O1CY ATTN DOCUMENT CONTROL

COMMANDER
U.S. ARMY MISSILE INTELLIGENCE AGENCY
REDSTONE ARSENAL, AL 35809
O1CY ATTN JIM GAMBLE

DIRECTOR
U.S. ARMY TRADOC SYSTEMS ANALYSIS
ACTIVITY
WHITE SANDS MISSILE RANGE, NM 89007
O1CY ATTN ATAA-SA
O1CY ATTN TCC/F. PAYAN JR.
O1CY ATTN ATTA-TAC LTC J. HESSE

COMMANDER
NAVAL ELECTRONIC SYSTEMS COMMAND
WASHINGTON, DC 20360
O1CY ATTN NAVALEX 034 T. HUGHES
O1CY ATTN PME 117
O1CY ATTN PME 117-T
O1CY ATTN CODE 5011

COMMANDING OFFICER
NAVAL INTELLIGENCE SUPPORT CTR
4301 SUITLAND ROAD, BLDG. 5
WASHINGTON, DC 20390
O1CY ATTN MR. DUBBIN STIC 12
O1CY ATTN NISC-50
O1CY ATTN CODE 5404 J. GALET

COMMANDER
NAVAL OCEAN SYSTEMS CENTER
SAN DIEGO, CA 92152
O1CY ATTN J. FERGUSON

NAVAL RESEARCH LABORATORY
WASHINGTON, DC 20375
O1CY ATTN CODE 4700 S.L. Ossakow,
26 CYS IF UNCLASS
(O1CY IF CLASS)
ATTN CODE 4780 J.D. HUBA, 50
CYS IF UNCLASS, O1CY IF CLASS
O1CY ATTN CODE 4701 I. VITKOVITSKY
O1CY ATTN CODE 7500
O1CY ATTN CODE 7550
O1CY ATTN CODE 7580
O1CY ATTN CODE 7551
O1CY ATTN CODE 7555
O1CY ATTN CODE 4730 E. MCLEAN
O1CY ATTN CODE 4752
O1CY ATTN CODE 4730 B. RIPIN
20CY ATTN CODE 2628

COMMANDER
NAVAL SPACE SURVEILLANCE SYSTEM
DAHLGREN, VA 22448
O1CY ATTN CAPT J.H. BURTON

OFFICER-IN-CHARGE
NAVAL SURFACE WEAPONS CENTER
WHITE OAK, SILVER SPRING, MD 20910
01CY ATTN CODE F31

DIRECTOR
STRATEGIC SYSTEMS PROJECT OFFICE
DEPARTMENT OF THE NAVY
WASHINGTON, DC 20376
01CY ATTN NSP-2141
01CY ATTN NSSP-2722 FRED WIMBERLY

COMMANDER
NAVAL SURFACE WEAPONS CENTER
DAHLGREN LABORATORY
DAHLGREN, VA 22448
01CY ATTN CODE DF-14 R. BUTLER

OFFICER OF NAVAL RESEARCH
ARLINGTON, VA 22217
01CY ATTN CODE 465
01CY ATTN CODE 461
01CY ATTN CODE 402
01CY ATTN CODE 420
01CY ATTN CODE 421

COMMANDER
AEROSPACE DEFENSE COMMAND/XPD
DEPARTMENT OF THE AIR FORCE
ENT AFB, CO 80912
01CY ATTN XPDQQ
01CY ATTN XP

AIR FORCE GEOPHYSICS LABORATORY
HANSCOM AFB, MA 01731
01CY ATTN OPR HAROLD GARDNER
01CY ATTN LKB
KENNETH S.W. CHAMPION
01CY ATTN OPR ALVA T. STAIR
01CY ATTN PHD JURGEN BUCHAU
01CY ATTN PHD JOHN P. MULLEN

AF WEAPONS LABORATORY
KIRTLAND AFT, NM 87117
01CY ATTN SUL
01CY ATTN CA ARTHUR H. GUENTHER

AFTAC
PATRICK AFB, FL 32925
01CY ATTN TN

AIR FORCE AVIONICS LABORATORY
WRIGHT-PATTERSON AFB, OH 45433
01CY ATTN AAD WADE HUNT
01CY ATTN AAD ALLEN JOHNSON

DEPUTY CHIEF OF STAFF
RESEARCH, DEVELOPMENT, & ACQ
DEPARTMENT OF THE AIR FORCE
WASHINGTON, DC 20330
01CY ATTN AFRDQ

HEADQUARTERS
ELECTRONIC SYSTEMS DIVISION
DEPARTMENT OF THE AIR FORCE
HANSCOM AFB, MA 01731-5000
01CY ATTN J. DEAS
ESD/SCD-4

COMMANDER
FOREIGN TECHNOLOGY DIVISION, AFSC
WRIGHT-PATTERSON AFB, OH 45433
01CY ATTN NICD LIBRARY
01CY ATTN ETD P. B. BALLARD

COMMANDER
ROME AIR DEVELOPMENT CENTER, AFSC
GRIFFISS AFB, NY 13441
01CY ATTN DOC LIBRARY/TSLD
01CY ATTN OCSE V. COYNE

STRATEGIC AIR COMMAND/XPFS
OFFUTT AFB, NB 68113
01CY ATTN XPFS

SAMSO/MN
NORTON AFB, CA 92409
(MINUTEMAN)
01CY ATTN MNNL

COMMANDER
ROME AIR DEVELOPMENT CENTER, AFSC
HANSCOM AFB, MA 01731
01CY ATTN EEP A. LORENTZEN

DEPARTMENT OF ENERGY
LIBRARY ROOM G-042
WASHINGTON, DC 20545
01CY ATTN DOC CON FOR A. LABOWITZ

DEPARTMENT OF ENERGY
ALBUQUERQUE OPERATIONS OFFICE
P.O. BOX 5400
ALBUQUERQUE, NM 87115
01CY ATTN DOC CON FOR D. SHERWOOD

EG&G, INC.
LOS ALAMOS DIVISION
P.O. BOX 809
LOS ALAMOS, NM 85544
01CY ATTN DOC CON FOR J. BREEDLOVE

UNIVERSITY OF CALIFORNIA
LAWRENCE LIVERMORE LABORATORY
P.O. BOX 808
LIVERMORE, CA 94550
01CY ATTN DOC CON FOR TECH INFO
DEPT
01CY ATTN DOC CON FOR L-389 R. OTT
01CY ATTN DOC CON FOR L-31 R. HAGER

LOS ALAMOS NATIONAL LABORATORY
P.O. BOX 1663
LOS ALAMOS, NM 87545
01CY ATTN DOC CON FOR J. WOLCOTT
01CY ATTN DOC CON FOR R.F. TASCHEK
01CY ATTN DOC CON FOR E. JONES
01CY ATTN DOC CON FOR J. MALIK
01CY ATTN DOC CON FOR R. JEFFRIES
01CY ATTN DOC CON FOR J. ZINN
01CY ATTN DOC CON FOR D. WESTERVELT
01CY ATTN D. SAPPENFIELD

LOS ALAMOS NATIONAL LABORATORY
MS D438
LOS ALAMOS, NM 87545
01CY ATTN S.P. GARY
01CY ATTN J. BOROVSKY

SANDIA LABORATORIES
P.O. BOX 5800
ALBUQUERQUE, NM 87115
01CY ATTN DOC CON FOR W. BROWN
01CY ATTN DOC CON FOR A.
THORNBROUGH
01CY ATTN DOC CON FOR T. WRIGHT
01CY ATTN DOC CON FOR D. DAHLGREN
01CY ATTN DOC CON FOR 3141
01CY ATTN DOC CON FOR SPACE PROJECT
DIV

SANDIA LABORATORIES
LIVERMORE LABORATORY
P.O. BOX 969
LIVERMORE, CA 94550
01CY ATTN DOC CON FOR B. MURPHEY
01CY ATTN DOC CON FOR T. COOK

OFFICE OF MILITARY APPLICATION
DEPARTMENT OF ENERGY
WASHINGTON, DC 20545
01CY ATTN DOC CON DR. YO SONG

NATIONAL OCEANIC & ATMOSPHERIC ADMIN
ENVIRONMENTAL RESEARCH LABORATORIES
DEPARTMENT OF COMMERCE
BOULDER, CO 80302
01CY ATTN R. GRUBB

DEPARTMENT OF DEFENSE CONTRACTORS

AEROSPACE CORPORATION
P.O. BOX 92957
LOS ANGELES, CA 90009
01CY ATTN I. GARFUNKEL
01CY ATTN T. SALMI
01CY ATTN V. JOSEPHSON
01CY ATTN S. BOWER
01CY ATTN D. OLSEN

ANALYTICAL SYSTEMS ENGINEERING CORP
5 OLD CONCORD ROAD
BURLINGTON, MA 01803
01CY ATTN RADIO SCIENCES

AUSTIN RESEARCH ASSOC., INC.
1901 RUTLAND DRIVE
AUSTIN, TX 78758
01CY ATTN L. SLOAN
01CY ATTN R. THOMPSON

BERKELEY RESEARCH ASSOCIATES, INC.
P.O. BOX 983
BERKELEY, CA 94701
01CY ATTN J. WORKMAN
01CY ATTN C. PRETTIE
01CY ATTN S. BRECHT

BOEING COMPANY, THE
P.O. BOX 3707
SEATTLE, WA 98124
01CY ATTN G. KEISTER
01CY ATTN D. MURRAY
01CY ATTN G. HALL
01CY ATTN J. KENNEY

CHARLES STARK DRAPER LABORATORY, INC.
555 TECHNOLOGY SQUARE
CAMBRIDGE, MA 02139
01CY ATTN D.B. COX
01CY ATTN J.P. GILMORE

COMSAT LABORATORIES
22300 COMSAT DRIVE
CLARKSBURG, MD 20871
01CY ATTN G. HYDE

CORNELL UNIVERSITY
DEPARTMENT OF ELECTRICAL ENGINEERING
ITHACA, NY 14850
01CY ATTN D.T. FARLEY, JR.

ELECTROSPACE SYSTEMS, INC.
BOX 1359
RICHARDSON, TX 75080
01CY ATTN H. LOGSTON
01CY ATTN SECURITY (PAUL PHILLIPS)

EOS TECHNOLOGIES, INC.
606 Wilshire Blvd.
Santa Monica, CA 90401
01CY ATTN C.B. GABBARD
01CY ATTN R. LELEVIER

GENERAL ELECTRIC COMPANY
SPACE DIVISION
VALLEY FORGE SPACE CENTER
GODDARD BLVD KING OF PRUSSIA
P.O. BOX 8555
PHILADELPHIA, PA 19101
01CY ATTN M.H. BORTNER
SPACE SCI LAB

GEOPHYSICAL INSTITUTE
UNIVERSITY OF ALASKA
FAIRBANKS, AK 99701
(ALL CLASS ATTN: SECURITY OFFICER)
01CY ATTN T.N. DAVIS (UNCLASS ONLY)
01CY ATTN NEAL BROWN (UNCLASS ONLY)

GTE SYLVANIA, INC.
ELECTRONICS SYSTEMS GRP-EASTERN DIV
77 A STREET
NEEDHAM, MA 02194
01CY ATTN DICK STEINHOF

HSS, INC.
2 ALFRED CIRCLE
BEDFORD, MA 01730
01CY ATTN DONALD HANSEN

ILLINOIS, UNIVERSITY OF
107 COBLE HALL
150 DAVENPORT HOUSE
CHAMPAIGN, IL 61820
(ALL CORRES ATTN DAN MCCLELLAND)
01CY ATTN K. YEH

INSTITUTE FOR DEFENSE ANALYSES
1801 NO. BEAUREGARD STREET
ALEXANDRIA, VA 22311
01CY ATTN J.M. AEIN
01CY ATTN ERNEST BAUER
01CY ATTN HANS WOLFARD
01CY ATTN JOEL BENGSTON

INTL TEL & TELEGRAPH CORPORATION
500 WASHINGTON AVENUE
NUTLEY, NJ 07110
01CY ATTN TECHNICAL LIBRARY

JAYCOR
11011 TORREYANA ROAD
P.O. BOX 85154
SAN DIEGO, CA 92138
01CY ATTN J.L. SPERLING

JOHNS HOPKINS UNIVERSITY
APPLIED PHYSICS LABORATORY
JOHNS HOPKINS ROAD
LAUREL, MD 20810
01CY ATTN DOCUMENT LIBRARIAN
01CY ATTN THOMAS POTEMRA
01CY ATTN JOHN DASSOULAS

KAMAN SCIENCES CORP
P.O. BOX 7463
COLORADO SPRINGS, CO 80933
01CY ATTN T. MEAGHER

KAMAN TEMPO-CENTER FOR ADVANCED
STUDIES
816 STATE STREET (P.O DRAWER QQ)
SANTA BARBARA, CA 93102
01CY ATTN DASIAK
01CY ATTN WARREN S. KNAPP
01CY ATTN WILLIAM MCNAMARA
01CY ATTN B. GAMBILL

LINKABIT CORP
10453 ROSELLE
SAN DIEGO, CA 92121
01CY ATTN IRWIN JACOBS

LOCKHEED MISSILES & SPACE CO., INC
P.O. BOX 504
SUNNYVALE, CA 94088
01CY ATTN DEPT 60-12
01CY ATTN D.R. CHURCHILL

LOCKHEED MISSILES & SPACE CO., INC.
3251 HANOVER STREET
PALO ALTO, CA 94304
01CY ATTN MARTIN WALT DEPT 52-12
01CY ATTN W.L. IMHOF DEPT 52-12
01CY ATTN RICHARD G. JOHNSON
DEPT 52-12
01CY ATTN J.B. CLADIS DEPT 52-12

MARTIN MARIETTA CORP
ORLANDO DIVISION
P.O. BOX 5837
ORLANDO, FL 32805
01CY ATTN R. HEFFNER

MCDONNELL DOUGLAS CORPORATION
5301 BOLSA AVENUE
HUNTINGTON BEACH, CA 92647
01CY ATTN N. HARRIS
01CY ATTN J. MOULE
01CY ATTN GEORGE MROZ
01CY ATTN W. OLSON
01CY ATTN R.W. HALPRIN
01CY ATTN TECHNICAL
LIBRARY SERVICES

MISSION RESEARCH CORPORATION
735 STATE STREET
SANTA BARBARA, CA 93101
01CY ATTN P. FISCHER
01CY ATTN W.F. CREVIER
01CY ATTN STEVEN L. GUTSCHE
01CY ATTN R. BOGUSCH
01CY ATTN R. HENDRICK
01CY ATTN RALPH KILB
01CY ATTN DAVE SOWLE
01CY ATTN F. FAJEN
01CY ATTN M. SCHEIBE
01CY ATTN CONRAD L. LONGMIRE
01CY ATTN B. WHITE
01CY ATTN R. STAGAT

MISSION RESEARCH CORP.
1720 RANDOLPH ROAD, S.E.
ALBUQUERQUE, NM 87106
01CY R. STELLINGWERF
01CY M. ALME
01CY L. WRIGHT

MITRE CORP
WESTGATE RESEARCH PARK
1820 DOLLY MADISON BLVD
MCLEAN, VA 22101
01CY ATTN W. HALL
01CY ATTN W. FOSTER

PACIFIC-SIERRA RESEARCH CORP
12340 SANTA MONICA BLVD.
LOS ANGELES, CA 90025
01CY ATTN E.C. FIELD, JR.

PENNSYLVANIA STATE UNIVERSITY
IONOSPHERE RESEARCH LAB
318 ELECTRICAL ENGINEERING EAST
UNIVERSITY PARK, PA 16802
(NO CLASS TO THIS ADDRESS)
01CY ATTN IONOSPHERIC RESEARCH LAB

PHOTOMETRICS, INC.
4 ARROW DRIVE
WOBBURN, MA 01801
01CY ATTN IRVING L. KOFISKY

PHYSICAL DYNAMICS, INC.
P.O. BOX 3027
BELLEVUE, WA 98009
01CY ATTN E.J. FREMOUW

PHYSICAL DYNAMICS, INC.
P.O. BOX 10367
OAKLAND, CA 94610
ATTN A. THOMSON

R & D ASSOCIATES
P.O. BOX 9695
MARINA DEL REY, CA 90291
01CY ATTN FORREST CILMORE
01CY ATTN WILLIAM B. WRIGHT, JR.
01CY ATTN WILLIAM J. KARZAS
01CY ATTN H. ORY
01CY ATTN C. MACDONALD
01CY ATTN BRIAN LAMB
01CY ATTN MORGAN GROVER

RAYTHEON CO.
528 BOSTON POST ROAD
SUDBURY, MA 01776
01CY ATTN BARBARA ADAMS

RIVERSIDE RESEARCH INSTITUTE
330 WEST 42nd STREET
NEW YORK, NY 10036
01CY ATTN VINCE TRAPANI

SCIENCE APPLICATIONS
INTERNATIONAL INCORPORATED
1150 PROSPECT PLAZA
LA JOLLA, CA 92037
01CY ATTN LEWIS M. LINSON
01CY ATTN DANIEL A. HAMLIN
01CY ATTN E. FRIEMAN
01CY ATTN E.A. STRAKER
01CY ATTN CURTIS A. SMITH

SCIENCE APPLICATIONS
INTERNATIONAL CORPORATION
1710 GOODRIDGE DR.
MCLEAN, VA 22102
01CY J. COCKAYNE
01CY E. HYMAN

SRI INTERNATIONAL
333 RAVENSWOOD AVENUE
MENLO PARK, CA 94025
01CY ATTN J. CASPER
01CY ATTN DONALD NEILSON
01CY ATTN ALAN BURNS
01CY ATTN G. SMITH
01CY ATTN R. TSUNODA
01CY ATTN DAVID A. JOHNSON
01CY ATTN WALTER G. CHESNUT
01CY ATTN CHARLES L. RINO
01CY ATTN WALTER JAYE
01CY ATTN J. VICKREY
01CY ATTN RAY L. LEADABRAND
01CY ATTN G. CARPENTER
01CY ATTN G. PRICE
01CY ATTN R. LIVINGSTON
01CY ATTN V. GONZALES
01CY ATTN D. MCDANIEL

TECHNOLOGY INTERNATIONAL CORP
75 WIGGINS AVENUE
BEDFORD, MA 01730
01CY ATTN W.P. BOQUIST

TRW DEFENSE & SPACE SYS GROUP
ONE SPACE PARK
REDONDO BEACH, CA 90278
01CY ATTN R. K. PLEBUCH
01CY ATTN S. ALTSCHULER
01CY ATTN D. DEE
01CY ATTN D/ STOCKWELL
SNTF/1575

VISIDYNE
SOUTH BEDFORD STREET
BURLINGTON, MA 01803
01CY ATTN W. REIDY
01CY ATTN J. CARPENTER
01CY ATTN C. HUMPHREY

UNIVERSITY OF PITTSBURGH
PITTSBURGH, PA 15213
01CY ATTN: N. ZABUSKY

Code 1220 lcp

Records lcp

Director of Research
U.S. Naval Academy
Annapolis, MD 21402 2cp

IONOSPHERIC MODELING DISTRIBUTION LIST
(UNCLASSIFIED ONLY)

PLEASE DISTRIBUTE ONE COPY TO EACH OF THE FOLLOWING PEOPLE (UNLESS OTHERWISE NOTED)

NAVAL RESEARCH LABORATORY
WASHINGTON, DC 20375

DR. H. GURSKY - CODE 4100
DR. J.M. GOODMAN - CODE 4180
DR. P. RODRIQUEZ - CODE 4750
DR. P. MANGE - CODE 4101
DR. R. MEIER - CODE 4140

A.F. GEOPHYSICS LABORATORY
L.G. HANSCOM FIELD
BEDFORD, MA 01731

DR. T. ELKINS
MRS. W. SWIDER
MRS. R. SAGALYN
DR. J.M. FORBES
DR. T.J. KENESHEA
DR. W. BURKE
DR. H. CARLSON
DR. J. JASPERSE
DR. F.J. RICH
DR. N. MAYNARD
DR. D.N. ANDERSON
DR. S. BASU

BOSTON UNIVERSITY
DEPARTMENT OF ASTRONOMY
BOSTON, MA 02215

DR. J. AARONS
DR. M. MENDILLO

CORNELL UNIVERSITY
ITHACA, NY 14850

DR. B. FEJER
DR. R. SUDAN
DR. D. FARLEY
DR. M. KELLEY

INSTITUTE FOR DEFENSE ANALYSIS
1801 N. BEAUREGARD STREET
ARLINGTON, VA 22311

DR. E. BAUER

MASSACHUSETTS INSTITUTE OF TECHNOLOGY
PLASMA FUSION CENTER
CAMBRIDGE, MA 02139
LIBRARY, NW16-262
DR. T. CHANG
DR. R. LINDZEN

NASA
GODDARD SPACE FLIGHT CENTER
GREENBELT, MD 20771
DR. N. MAYNARD (CODE 696)
DR. R.F. BENSON
DR. K. MAEDA
DR. S. CURTIS
DR. M. DUBIN

COMMANDER
NAVAL OCEAN SYSTEMS CENTER
SAN DIEGO, CA 92152
MR. R. ROSE - CODE 5321

NOAA
DIRECTOR OF SPACE AND
ENVIRONMENTAL LABORATORY
BOULDER, CO 80302
DR. A. GLENN JEAN
DR. G.W. ADAMS
DR. K. DAVIES
DR. R.F. DONNELLY

OFFICE OF NAVAL RESEARCH
800 NORTH QUINCY STREET
ARLINGTON, VA 22217
DR. G. JOINER

LABORATORY FOR PLASMA AND
FUSION ENERGIES STUDIES
UNIVERSITY OF MARYLAND
COLLEGE PARK, MD 20742
JHAN VARYAN HELLMAN,
REFERENCE LIBRARIAN

PENNSYLVANIA STATE UNIVERSITY
UNIVERSITY PARK, PA 16802

DR. J.S. NISBET
DR. P.R. ROHRBAUGH
DR. L.A. CARPENTER
DR. M. LEE
DR. R. DIVANY
DR. P. BENNETT
DR. E. BLEVANS

PRINCETON UNIVERSITY
PLASMA PHYSICS LABORATORY
PRINCETON, NJ 08540
DR. F. PERKINS

SAIC
1150 PROSPECT PLAZA
LA JOLLA, CA 92037
DR. D.A. HAMLIN
DR. L. LINSON
DR. E. FRIEMAN

SRI INTERNATIONAL
333 RAVENSWOOD AVENUE
MENLO PARK, CA 94025
DR. R. TSUNODA
DR. WALTER CHESNUT
DR. CHARLES RINO
DR. J. VICKREY
DR. R. LIVINGSTON

STANFORD UNIVERSITY
STANFORD, CA 94305
DR. P.M. BANKS
DR. R. HELLIWELL

U.S. ARMY ABERDEEN RESEARCH
AND DEVELOPMENT CENTER
BALLISTIC RESEARCH LABORATORY
ABERDEEN, MD
DR. J. HEIMERL

GEOPHYSICAL INSTITUTE
UNIVERSITY OF ALASKA
FAIRBANKS, AL 99701
DR. L.C. LEE

UTAH STATE UNIVERSITY
4TH AND 8TH STREETS
LOGAN, UT 84322
DR. R. HARRIS
DR. K. BAKER
DR. R. SCHUNK
DR. J. ST.-MAURICE
DR. N. SINGH

UNIVERSITY OF CALIFORNIA
LOS ALAMOS NATIONAL LABORATORY
EES DIVISION
LOS ALAMOS, NM 87545
DR. M. PONGRATZ, ESS-DOT
DR. D. SIMONS, ESS-7, MS-D466
DR. L. DUNCAN, ESS-7, MS-D466
DR. P. BERNHARDT, ESS-7, MS-D466
DR. S.P. GARY, ESS-8
DENNIS RIGGIN, ATMOS SCI GRP

UNIVERSITY OF ILLINOIS
DEPARTMENT OF ELECTRICAL ENGINEERING
1406 W. GREEN STREET
URBANA, IL 61801
DR. ERHAN KUDEKI

UNIVERSITY OF CALIFORNIA,
LOS ANGELES
405 HILLGARD AVENUE
LOS ANGELES, CA 90024
DR. F.V. CORONITI
DR. C. KENNEL
DR. A.Y. WONG

UNIVERSITY OF MARYLAND
COLLEGE PARK, MD 20740
DR. K. PAPADOPOULOS
DR. E. OTT

JOHNS HOPKINS UNIVERSITY
APPLIED PHYSICS LABORATORY
JOHNS HOPKINS ROAD
LAUREL, MD 20810
DR. R. GREENWALD
DR. C. MENG
DR. T. POTEMRA

UNIVERSITY OF PITTSBURGH
PITTSBURGH, PA 15213
DR. N. ZABUSKY
DR. M. BIONDI
DR. E. OVERMAN

UNIVERSITY OF TEXAS AT DALLAS
CENTER FOR SPACE SCIENCES
P.O. BOX 688
RICHARDSON, TX 75080
DR. R. HEELIS
DR. W. HANSON
DR. J.P. McCLURE

END

DATE

FILMED

MARCH

1988

DTIC